Journal Of Geophysical Research-oceans
August 2016, Volume 121 Issue 8 Pages 5549-5569
https://doi.org/10.1002/2015JC011542
https://archimer.ifremer.fr/doc/00347/45831/

Dense water formation in the north-western Mediterranean area during HyMeX-SOP2 in 1/36° ocean simulations: Sensitivity to initial conditions

Léger Fabien [1, *], Brossier Cindy Lebeaupin [1], Giordani Hervé [1], Arsouze Thomas [2, 3], Beuvier Jonathan [4, 5], Bouin Marie-Noëlle [1], Bresson Emilie [1, 6, 7], Ducrocq Véronique [1], Fourrie Nadia [1], Nuret Mathieu [1]

[1] CNRS Meteofrance, Ctr Natl Rech Meteorol CNRM UMR3589, Toulouse, France.
[2] Univ Paris Saclay, Ecole Natl Super Tech Avancees ParisTech, Palaiseau, France.
[3] CNRS UPMC Ecole Polytech ENS, Lab Meteorol Dynam LMD UMR8539, Palaiseau, France.
[4] Mercator Ocean, Ramonville St Agne, France.
[5] Meteo France, Toulouse, France.
[6] Univ Quebec, Montreal, PQ, Canada.
[7] Ouranos Consortium, Montreal, PQ, Canada.

* Corresponding author : Fabien Léger, email address : fabien.leger@meteo.fr

Abstract :

The north-western Mediterranean Sea is a key location where intense air-sea exchanges occur in autumn and winter. The succession of strong mistral and tramontane situations, leading to significant evaporation and ocean heat loss, is well known as the controlling factor in the dense water formation (DWF) with deep convection episodes. During HyMeX-SOP2 (1 February to 15 March 2013), several platforms sampled the area in order to document DWF and air-sea exchanges. This study investigates the ability of the NEMO-WMED36 ocean model (1/36°-resolution), driven in surface by the hourly air-sea fluxes from the AROME-WMED forecasts (2.5 km resolution), to represent DWF during HyMeX-SOP2 and focuses on the sensitivity to initial conditions. After a short evaluation of the atmospheric forcing, the high-resolution oceanic simulations using three different data sets as initial and boundary conditions are compared to observations collected during the field campaign. It evidences that using regional model outputs may lead to unrealistic thermohaline characteristics for the intermediate and deep waters, which degrade the simulated new dense water formed. Using ocean analyses built from observations, permits to obtain more realistic characteristics of the Western Mediterranean dense water. However, a low stratification favors an overestimation of the convective area and of the DWF rate. The DWF chronology is also impacted. Nevertheless, in every run, SOP2 is characterized by the production of water denser than 29.11 kg m−3 with a peak during the strong mistral event of 23–25 February followed by a period of restratification, before a last event of bottom convection on 13–15 March.

Key Points:

► Three high-resolution ocean simulations are compared to HyMeX SOP2 observations ► The NEMO-WMED36 model is able to reproduce dense water formation during winter 2013. ► The large sensitivity of dense water formation to initial conditions is highlighted

1. Introduction

The Mediterranean basin is characterized by a pronounced orography around its perimeter and is prone to local intense meteorological events, such as strong local winds (bora, mistral, tramontane, etc.) [*Zecchetto and De Biaso*, 2007]. These winds, which are generally enhanced and channeled by the surrounding orography, bring continental dry and cold air over the sea, inducing strong air-sea interactions with intense heat and momentum exchanges [*Flamant*, 2003; *Lebeaupin Brossier and Drobinski*, 2009; *Small et al.*, 2012].

The north-western Mediterranean Sea is a key location where intense air-sea exchanges occur. Indeed, the mistral and tramontane, northerly and north-westerly wind, respectively, frequently affect this area and drive the horizontal ocean circulation and the exchanges between the coastal area and the open-sea. In this location, the ocean circulation is mainly in the form of a cyclonic gyre [*Millot*, 1999; *Millot and Taupier-Letage*, 2005] with Atlantic Water (AW: >14 °C and ∼38 psu) in the upper part, above Levantine Intermediate Water (LIW: 13.4-13.5 °C and 38.55 psu), itself above Western Mediterranean Deep Water (WMDW: 12.9 °C and 38.485 psu). At the beginning of winter, the Western Intermediate Water (WIW: ∼12.4 °C, ∼38 psu) can also be found in the north-western Mediterranean area.

Several small-scale oceanic processes affect the Gulf of Lion (GoL), where bathymetry is characterized by a continental shelf bounded by a very steep slope and several submarine canyons: coastal upwelling and downwelling [*Millot*, 1979, 1982], shelf-water cascading [*Dufau-Julliand et al.*, 2004; *Canals et al.*, 2006], eddies, intrusions or meanders of the Northern Current [*Ourmières et al.*, 2011], freshwater plumes from the Rhône

river [*Estournel et al.*, 2001]. The north-western Mediterranean Sea is finally filled by (sub)mesoscale oceanic patterns (eddies, submesoscale coherent vorticies and filaments), highly sensitive to the winter-time atmospheric conditions. The succession of strong-wind events in winter is indeed well known as the major factor in the Dense Water Formation (DWF) in the western Mediterranean [*Schott et al.*, 1996; *Marshall and Schott*, 1999] with deep convection episodes that play a significant role in the thermohaline circulation. WIW can also sink to ∼150 m depth (between the AW and the LIW) under strong wind events [*Gasparini et al.*, 1999; *Juza et al.*, 2013].

To resolve such mesoscale patterns, an ocean model should have a grid-mesh with an horizontal resolution lower than the first Rossby deformation radius (R_d), which is estimated from the Medar/MedAtlas database [*MEDAR/MEDATLAS Group*, 2002] to be about 10 km in the Mediterranean Sea, between 8 and 10 km in the GoL, 2 to 3 km above the continental shelf [*Beuvier et al.*, 2012]. To drive such ocean models, atmospheric forcing with high resolution in space and time is mandatory to represent the complex ocean circulation in the region [*Castellari et al.*, 2000; *Herrmann and Somot*, 2008; *Béranger et al.*, 2010; *Lebeaupin Brossier et al.*, 2012].

The HyMeX project (*Hydrological cycle in the Mediterranean Experiment*) [*Drobinski et al.*, 2014] investigates the hydrological cycle in the Mediterranean region, from intense events (heavy precipitation, floods, strong winds with intense air-sea fluxes) to regional climate. The second Special Observations Period (SOP2) over the north-western Mediterranean area in February-March 2013 [*Estournel et al.*, 2016] was dedicated to the documentation of the DWF. The main objective of the field campaign was to better understand the fine scale processes involved in the DWF and ocean deep convection and to

examine the role of intense air-sea fluxes events. Several platforms were deployed in the north-western Mediterranean Sea during SOP2, offering a quite unique wide cover of the area. The observation dataset includes in particular drifting buoys, Argo floats, gliders, and XBT and CTD profiles from several ships. This large amount of data represents a challenging opportunity to examine the accuracy of the ocean models to represent such phenomena.

The goal of this study is to evaluate the DWF representation in the NEMO-WMED36 model with a spatial resolution of ∼2.2-2.5 km, driven by high-resolution high-frequency atmospheric fluxes. The initial and boundary conditions impact is examined by using three different datasets: outputs of a free high-resolution regional ocean model (NEMO-MED36), analysed fields from the Mercator Océan PSY2 operational system, and a mixed analysed product (Optimal Interpolation of the MOOSE campaign in summer 2012 combined to the PSY2 analyses).

The numerical experiments as the in-situ dataset used for validation are presented in sections 2 and 3. After an analysis of the high-resolution high-frequency atmospheric forcing used in section 4, we evaluate the accuracy of the high-resolution ocean model compared to SOP2 observations in section 5. The description and evaluation of the DWF is done in section 6. Discussions and conclusion are finally given (section 7).

2. Numerical experiments

2.1. The high-resolution ocean model: NEMO-WMED36

The numerical code for the ocean is NEMO [*Madec*, 2008], and is used in a sub-regional eddy-resolving western Mediterranean configuration (Fig. 1) with a 1/36° horizontal resolution over a tripolar ORCA-grid (∼2.2-2.5 km, the horizontal resolution becomes

finer with increasing latitudes) called WMED36 [*Lebeaupin Brossier et al.*, 2014]. In the vertical, 50 stretched z-levels are used. The vertical level thickness is 1 m in surface and 400 m at the sea bottom (*i.e.* at 4000 m depth). The model has two radiative open boundaries: one west boundary at ∼4.8°W (60km east of the Strait of Gibraltar), one south boundary accross the Sicily Channel (∼37°N). The Strait of Messina between Sicily and Italy is closed.

The horizontal eddy viscosity coefficient is fixed to -1×10^9 $m^2.s^{-1}$ for the dynamics (velocity) with the use of a bi-Laplacian operator. The TVD scheme is used for tracer advection in order to conserve energy and enstrophy [*Barnier et al.*, 2006]. The vertical diffusion is performed by the standard turbulent kinetic energy model of NEMO [*Blanke and Delecluse*, 1993]. The convection is parameterized by an increase in the vertical diffusion [*Lazar et al.*, 1999] by 10 $m^2.s^{-1}$ in case of instabilities. The filtered free surface of *Roullet and Madec* [2000] is used to keep the sea volume constant. A no-slip condition is applied at the bottom and the bottom friction is parameterized by a quadratic function with a coefficient depending on the 2D mean tidal energy [*Lyard et al.*, 2006; *Beuvier et al.*, 2012].

2.2. Surface forcing

For each simulation, WMED36 is driven at the air-sea interface by the heat (Q=SW-LW-H-LE, short-wave minus long-wave minus sensible minus latent heat fluxes), freshwater (F=E-P, evaporation minus precipitation) and momentum fluxes ($\vec{\tau}$), taken from the AROME-WMED hourly forecast (*doi:10.6096/HYMEX.AROME_WMED.2012.02.20*). The non-hydrostatic and convection-permitting AROME-WMED model [*Fourrié et al.*, 2015] with a 2.5 km-resolution grid was dedicated to the HyMeX field campaigns, doing

in real-time daily forecasts from the beginning of the first HyMeX Special Observations Period (SOP1, from 5 September 2012 [*Ducrocq et al.*, 2014]) to the end of SOP2 (15 March 2013). Except its domain which covers the whole western Mediterranean Sea, AROME-WMED uses a similar configuration than AROME-France [*Seity et al.*, 2011]. In particular, in AROME-WMED, the first atmospheric level is at ∼10 m height. The radiative schemes are: the six spectral bands scheme from *Fouquart and Bonnel* [1980] for short-wave radiation (SW) and the Rapid Radiative Transfert Model (RRTM) [*Mlawer et al.*, 1997] for long-wave radiation (LW). The sea surface turbulent fluxes ($\vec{\tau}$, H and LE=$\mathcal{L}\times$E) are computed within the externalized surface scheme, called SURFEX [*Masson et al.*, 2013], and obtained with the ECUME parameterization [*Belamari*, 2005; *Belamari and Pirani*, 2007].

The runoffs are prescribed from a climatology [*Beuvier et al.*, 2010] and applied locally as a freshwater input in surface.

2.3. Initial and boundary conditions

We perform three sensitivity experiments, covering the two SOPs, using three different ocean datasets to initialise the thermohaline conditions and constrain the open boundaries (Tab. 1). Ocean is initially at rest.

In the reference experiment (IM36, see Tab. 1), the initial conditions for 3D potential temperature (θ) and salinity (S) are provided by the regional (NEMO-)MED36 simulation [*Arsouze et al.*, 2013] driven by the ARPERA forcing [*Herrmann and Somot*, 2008], with the monthly (August) means of θ and S. The open boundary conditions are taken from the same MED36 simulation, with monthly fields of θ, S, U and V, *i.e.* the water inputs and outputs across the Gibraltar Strait and the Sicily Channel are controlled by the boundary

conditions. The simulation begins on 15 August 2012, with a 15-day spin-up during which the surface forcing conditions are low and constant in space and time. From 31 August 2012 to 15 March 2013, WMED36 is driven at the air-sea interface by AROME-WMED hourly forecast. The results of this reference simulation over SOP1 in fall 2012 are fully described in *Lebeaupin Brossier et al.* [2014].

In the IPSY experiment (Tab. 1), the boundary conditions come from the PSY2V4R4 daily analyses averaged monthly. The PSY2 operational system of Mercator Océan [*Lellouche et al.*, 2013] has a 1/12° resolution and covers the north-east Atlantic Ocean, the North and Baltic Seas and the Mediterranean Sea. The initial conditions come from the 1 September 2012 PSY2V4R4 analysis. IPSY is driven at the air-sea interface by AROME-WMED hourly forecast from 1 September 2012 to 15 March 2013. This simulation begins without spin-up. Indeed, the spin-up procedure was not re-applied in IPSY as, first, we saw in IM36 that only the mixed layer of 10 to 30 m depth is affected by the 15-day analytic atmospheric forcing. The currents at depth ajust very rapidly to the ocean structures found in the initial state (not shown). The benefit is that IPSY only considers a realistic atmospheric forcing all the simulation long. Secondly, we only study here the simulations from the end of January 2013 (*i.e.* the first five months of simulation could be considered as a spin-up).

The IMAP experiment (Tab. 1) has the same boundary conditions than IPSY. IMAP also begins without spin-up and is driven at the air-sea interface by AROME-WMED hourly forecast from 1 September 2012 to 15 March 2013. The initial conditions were built with the PSY2V4R4 analysis of 1 August 2012 except in the north-western Mediterranean Sea, over a domain between 40°N-44°N and 2°E-12°E, where the analysed fields of the

MOOSE campaign are used. This campaign took place from 18 July to 5 August 2012 onboard of the Research-Vessel *Le Suroît*. The analysed fields, built in the frame of the ASICS-Med project are obtained first interpolating the observations from CTD profiles in addition to Argo floats, gliders and also Sea Surface Temperature (SST) from satellite radiometers and Lion and Azur buoys onto 800 vertical levels (of 5 m vertical resolution from near surface to bottom. First level at 1m depth) and then objectively analyzed onto a 1/12º horizontal grid for all vertical levels following the procedure used by *Giordani et al.* [2005]. The first guess of the analyses were derived from the temperature and salinity PSY2V4R4 analysis of Mercator. At each grid point, PSY2V4R4 was corrected using observations which lie within one influence time/space radius around the grid point, following the procedure of *De Mey and Ménard* [1989]. A space correlation radius of 10 km, consistent with the mesoscale structures, and a decay e-folding time of 1 day were chosen. The ASICS-MOOSE analysed fields are convenient to start the IMAP simulation on 1 September, as only the very thin (∼10 to 30 m depth) mixed layer varies in August (not shown).

At the beginning of September 2012, the three initial states differ in their stratification and characteristics (see section 5). MED36 simulation is a 14-year free regional run (not constrained by observations). It provides a balanced ocean state and contains very fine structures thanks to its 1/36°-resolution. On the other hand, PSY2 and the MOOSE-ASICS analyses are both closer to observations thanks to data assimilation. The MOOSE-ASICS product assimilates the largest amount of data and thus contains the most realistic conditions in the intermediate and bottom layers in the convective area (around the GoL), which is mandatory to well simulate the characteristics of the new dense water. Except

in the surface layer, the main differences found between the initial states largely persist till January (just before SOP2) when comparing IM36, IPSY and IMAP.

3. In-situ dataset from the HyMeX SOP2

A detailed description of the observing platforms deployed during SOP2 is presented in *Estournel et al.* [2016]. Only a summary is given in this section.

Two Météo-France moored buoys, Lion and Azur buoys, are located at 4.7^{o}E-42.1^{o}N and 7.8^{o}E-43.8^{o}N, respectively. They measure atmospheric data (2 m temperature, humidity, 10 m wind speed, direction and gust intensity, mean sea level pressure) and sea surface parameters (SST, waves height and period). The platform instrumentation was reinforced for the HyMeX campaign with radiative fluxes measurements, raingauges and a thermobathymetric chain giving the ocean upper-layer temperature between 0 and 250 m depth.

Glider platforms give 0-1000 m profiles along repeated sections. Among the five gliders sailing in the SOP2 area, two were particularly devoted to the convective zone: Campe did sections from Marseille [5.2°E-43.1°N] to north of Menorca [4.5°E-41°N] and Milou did sections crossing in the Lion buoy location [4.7°E-42.1°N], to Catalonia [3.5°E-41.6°N], to Banyuls [3.5°E-42.5°N] and to west of Sardinia [6.8°E-40.2°N].

Up to 17 Argo floats sailed in the western Mediterranean Sea during SOP2. They performed repeatedly 0-2000 m profiles (here we only consider tracers θ/S). Among them, four Argo floats located around the GoL made daily profiles. In this study, we use nearly 180 deep profiles available during SOP2 in the Argo dataset.

About 80 CTD profiles were also collected during SOP2, coming from various cruises done by the Reasearch-Vessels *Le Suroît* and *Téthys II* and the Port-Tender *Le Provence*.

The CTD profiles were carried out in the north-western Mediterranean Sea till seafloor, which means that the CTD dataset contains information about the very deep water in the north-western Mediterranean Sea (below 2000 m depth).

The main objective of this study is to investigate the representation in the three companion simulations of the water column evolution during HyMeX-SOP2. So, to fully describe the north-western Mediterranean Sea evolution till bottom, the comparison to the deep profiles collected with Argo floats and CTDs is preferentially presented here. The variability is also analysed thanks to comparisons with high-frequency sea surface data.

During HyMeX SOP2, several *Intensive Observations Periods* (IOPs) were defined according to atmosphere and ocean forecasts, in order to coordinate operations and the launches of new observing platforms. Three kinds of event were examined with IOPs: strong wind event, strong sea state and dense water formation/spreading. An additional IOP was done in order to coordinate the P/T *Le Provence* mission (IOP27: from 7 to 10 March 2013).

We examine, in the following, the atmospheric marine low-level conditions forecasted by AROME-WMED over the DWF area, in particular during strong wind events. The list of the strong wind event IOPs during HyMeX-SOP2 and of their main characteristics is summarized in Table 2.

4. Atmospheric conditions in AROME-WMED forecasts and forcing

The AROME-WMED forcing along the SOP2 is built from the 48 h-forecasts run each day in real-time. In fact, we concatenate the fields forecasted each day for the 1-24 h ranges (beginning of the forecast is 00 UTC). The time-series obtained for meteorological

parameters at the Lion buoy location are shown in Figure 2 and compared with observations.

The 2 m temperature time-serie is quite in good agreement with observations, except for the coldest values that are not well reproduced in AROME-WMED. Over the whole SOP2, the correlation is 0.95 and the bias is +0.48 °C. The maximum difference is found for 24 February 2013 (IOP24, Tab. 2), when the buoy observed 3.1 °C, whereas the simulated minimum 2 m temperature is 5.2 °C. The wind direction and intensity are also well represented in AROME-WMED. The correlation between the observed and simulated 10 m wind speed time-series is 0.94. The maximum differences are found for strong wind events (IOP21a, IOP24, IOP28, Tab. 2), with an overestimation (up to 3.5 $m.s^{-1}$) of the intensity in the forecast. The simulated humidity has a mean bias of -6 % over SOP2, but the correlation between the modelled and observed time-series is 0.84, showing the good representation of the chronology. The maximum differences (*i.e.* maximum underestimations) are found during the strongest wind events (IOP21a, IOP21c, IOP24, IOP28) associated with severe mistral and tramontane events.

The corresponding air-sea fluxes obtained in the AROME-WMED forecasts are presented in Figure 3. The momentum flux (τ, Fig. 3a) evidences the strong wind periods occurring during SOP2 over the GoL and summarized in Table 2. The maximum wind stress intensity is reached during IOP28 (14 March) with τ=1.6 $N.m^{-2}$ at Lion. The turbulent heat fluxes, i.e. H and LE, evidence less strong events (Fig. 3b). In fact, IOP25 (1 to 3 March) and IOP26 (4 to 7 March) are not mistral event but respectively north-easterly and strong easterly/south-easterly wind associated (Tab. 2) with precipitation. The freshwater (F) flux (Fig. 3c) computed as the difference between evaporation and

precipitation, shows the same distinction between intense northerly and north-westerly wind, *i.e.* mistral and tramontane regime, associated with large evaporation (IOP21a, IOP21c, IOP24 and IOP28 with positive value of F) and strong wind associated with relatively warm low-level air mass and precipitating systems (IOP25 and IOP26, negative values of F).

Figure 4 illustrates these two different strong wind regimes encountered during SOP2. Indeed, IOP26 (Fig. 4a) is characterized by a easterly/south-easterly low-level wind situation, which brings a humid and warm air mass over the north-western Mediterranean Sea (T2M=13 °C and RH2M=98 % at Lion, Fig. 2). Thus, despite the strong wind (up to 20 m.s^{-1} at Lion, Fig. 2), the net heat flux is generally small in the AROME-WMED forecast (H$\simeq$-100 W.m^{-2} and LE$\simeq$-200 W.m^{-2} at Lion). Moreover, the GoL is affected by large precipitation which compensates evaporation and finally brings freshwater to the superficial ocean. At the opposite, IOP28 is a typical situation of intense mistral (10 m wind up to nearly 30 m.s^{-1}) affecting a wide area of the western Mediterranean. It brings cold and dry air at low level (T2M=6 °C and RH2M=48 % at Lion, Fig. 2). This produces huge heat losses (Q$\leq$-1000 W.m^{-2}, Fig. 4b) and evaporation over the north-western Mediterranean area.

To sum up, the AROME-WMED short-range (0-24 h) forecasts produce an accurate description of the low-level meteorological conditions and of their high-frequency variability during SOP2 in the GoL. Compared to the Lion buoy, the biases are small except for major mistral events, when the atmospheric model produces too strong wind (overestimation up to +3.5 m.s^{-1}) and is not able to reach the coldest observed air temperature values (below 6 °C). The same defaults were evidenced by *Rainaud et al.* [2015] who

evaluated the AROME-WMED forecasts over sea during HyMeX-SOP1. The biases are smaller when comparing the forecasts to the Azur buoy observations which is farther from the mistral influence (not shown). The flux time-series show well the occurence of two different regimes during SOP2: (i) a predominant regime during mistral and tramontane events with large wind stress and heat and water losses and (ii) strong wind stress but low to moderate heat flux and negative or null freshwater flux associated with south/easterly moist and warm low-level jet and precipitation over sea.

5. Comparison against SOP2 observations

In this section, the WMED36 simulations, all driven by the AROME-WMED forecasted fluxes, are compared to some of the in-situ observations collected during SOP2. For each simulation, the data are colocalized in space and time taking the nearest grid point at the closest time step in the NEMO-WMED36 outputs.

First, the three sensitivity experiments are compared to Argo profiles. For density, to be coherent with NEMO-WMED36 outputs, the state formula of *Jackett and McDougall* [1994] is applied to the Argo profiles, as potential temperature and salinity are observed. Figure 5 shows the mean vertical biases in temperature, salinity and density. The IM36 simulation presents the largest biases. The upper layer (0-200 m) is too cold (-0.4 °C) and the salinity is significantly underestimated (-0.2 psu). On the contrary, IM36 is a little too warm (+0.04 °C) and the salinity is overestimated (+0.02 psu) in the intermediate layer (200-400 m). The deep layer (400-2000 m) shows again negative biases in both temperature and salinity. As for the density, stratification in IM36 is overestimated when compared to observations with light water in surface, to dense intermediate water and slightly denser than observations in the deep layer. IM36 present cases of bias com-

pensation in the deep layer, where despite strong negative temperature and salinity bias, the density bias is nearly null. IPSY shows a density bias inversion at around 800 m depth with too light water in the upper part and too dense in the deep layer. At 2000 m depth, the density bias is +0.008 kg.m^{-3}, associated with a positive bias in salinity (+0.01 psu). The salinity is significantly underestimated in the 0-200 m layer (-0.08 psu) in IPSY and the temperature is overestimated at all levels (up to +0.07 °C at 300 m. IMAP presents the lowest biases, which are almost null below 400 m. In the surface layer the temperature and salinity are underestimated, by -0.2 °C and by -0.04 psu, respectively. The comparison to the Milou glider profiles highlights the same differences between the three companion simulations with the same sign of the biases against observations in the near-surface, intermediate and deep (till 1000 m) layers (not shown).

Figure 6 presents for each simulation the spatial distribution of biases averaged over the water column in the north-western Mediterranean area for temperature, salinity, and density, compared to Argo profiles and CTDs done on board of R/V *Le Suroît*. The vertical averaging method used here can induce artificial reduction by bias compensation between the different layers of the water column. It confirms that IMAP is the closest simulation from in-situ observations, despite some larger biases locally along the northern coasts, near Menorca and in the Balearic front area. IPSY is too warm and slightly too salty in the center of the GoL, and, too warm and not salty enough along the northern coasts. IM36 presents almost homogenous negative biases in both temperature and salinity. Only the south-western part and the area along the northern coasts show positive biases in temperature, and, only two profiles east of Menorca show positive biases in salinity. For the three simulations, the largest biases are located at the periphery of the convective

patch, showing there is a complex circulation with a large variability of the thermohaline characteristics in these areas, which is difficult to capture in the model. Moreover, the weekly root mean square error decreases along SOP2 for the three simulations (not shown) because of (i) the homogeneization of the simulated water column by mixing and (ii) an increase of the number of observed mixed vertical profiles associated with the enhancement of the convection. The comparison to gliders (not shown) gives the same results and confirms the spatial distribution of the biases in the north-western Mediterranean basin highlighted in Figure 6.

The comparison to the surface data collected by the Lion buoy (*SST doi:10.6096/HyMeX.LionBuoy.Thermosalinograh.20100308 and SSS doi:10.6096/MISTRALS-HyMeX-MOOSE.1025*) in Figure 7, evidences that IM36 has strong negative biases at the beginning of SOP2. The biases are linked to a very strong stratification which is not broken. The biases are indeed reduced when strong mixing occurs, first during IOP21d (9-11 February), then from 20 February and during IOP24 (23-26 February) when deep convection occurs. A period of restratification is simulated between 2 and 12 March, in coherence with observations (Fig. 7), before a last strong mixing event during IOP28 (13-15 March). IPSY shows almost the same behavior than IM36, with also a large stratification of the water column at the beginning of SOP2. Note that in IPSY the first strong mixing during IOP21d entrains intermediate water in the mixed layer, leading to positive biases in SST and SSS. Then, when the convection reaches the deep layer the biases in surface are almost null. In IMAP, the intermediate and deep convection begin sooner than in the two other experiments, on 2 February (IOP21a) and 6 February (IOP21b), respectively. The simulated SST and SSS of IMAP are in good agreement with the Lion buoy observations,

except during the restratification period, when a fine-scale eddy coming from the south bring colder and less salty waters in the near surface layer (not shown).

To better characterize the stratification during SOP2, we compute the vertical Index of Stratification (IS) [*Beuvier et al.*, 2010; *Adloff et al.*, 2015]. IS represents the potential energy of the water colomn of depth h which has to be destroyed by the surface buoyancy flux to obtain an homogeneous density profile. The higher the index is, the stronger the stratification is. IS is calculated using the following formula:

$$IS(x,y,h) = \int_0^{h(x,y)} N^2(x,y,z) z dz,$$

where N is the Brunt-Väisälä frequency ($N^2 = \frac{g}{\rho}\frac{\partial \rho}{\partial z}$), z the depth and (x,y) the grid point. h is either equal to the bottom depth or to 1000 m when the seafloor is deeper than 1000 m. Figure 8 displays the IS biases compared to the Argo floats and R/V *Le Suroît* CTD profiles for the three experiments. IS confirms that IPSY is too vertically stratified. IMAP performs better, however it presents a lack of stratification in the eastern part of the basin (west of Corsica and Sardinia). Near the Lion buoy, IMAP shows the best results with the lowest biases. In terms of chronology, IPSY and IM36 are too stratified at the beginning of the period, whereas IMAP has an accurate stratification compared to in-situ data. For the three simulations, SOP2 starts with a decrease of IS until the end of February, before a phase of restratification in March when IS increases, followed by a new short period of convection at the end of the SOP2, as seen in the observations.

Thus, the comparison to SOP2 observations in the north-western Mediterranean Sea shows that IMAP has the most realistic θ/S characteristics. This is inherited from the initial conditions which are very close to in-situ observations in the MOOSE-ASICS analysis. On the contrary, IM36 which begins from an ocean state obtained with a free regional

climate simulation, is further from observations. The stratification which is stronger in IM36 and IPSY with too dense water in the intermediate and deep layers strongly impacts the convection chronology. It occurs between two and three weeks before in IMAP near Lion buoy (around the 25 January 2013), compared to IM36 and IPSY. Looking at the Argo dataset, the Argo 6901470 situated close to the Lion buoy location shows an homogenous water column in density up to 2000 m from the 31 January 2013, attesting the deep convection occured at this place.

6. Dense water formation

The objective here is to evaluate the sensitivity of DWF to the initial conditions, according to the sensitivity experiments and to draw a preliminary budget of the dense water formed during HyMeX SOP2, from the solutions obtained with the WMED36 simulations.

First, we examine the simulated mixed layer depths (MLDs), computed from a density criteria. Indeed, the MLD is defined as the depth with a density gradient with the surface of 0.01 kg.m^{-3}. Figure 9 shows the colocalized comparison of the three sensitivity experiments to the "observed" MLD computed with the same density criteria from in-situ profiles (Argo floats and CTD profiles of R/V *Le Suroît*). IM36 and IPSY seem to underestimate the deep mixed profiles compared to observations. However, they both present a deep convective area (ocean mixed layer deeper than 2000 m) in the GoL in good agreement with several past studies and with sizes in the range of the convective patch interannual variability [*Madec et al.*, 1991; *Mertens and Schott*, 1998; *Herrmann and Somot*, 2008; *Béranger et al.*, 2010; *Beuvier et al.*, 2012]. The deep-convective area is more extended westwards in IM36 than IPSY. The evolution of the isopycnal surface depths and of the dense water volumes (Fig. 10, 11 and 12) highlights the scenario of

the convection simulated. Before SOP2, on 15 January 2013, IM36 and IPSY show the presence of large volumes of dense water (2.1 and 2.0×10^6 km^3 of water denser than 29.11 kg.m^{-3} in the north-western Mediterranean [between 40-44.5°N and 0-9°E], respectively, Fig. 12), with a doming of isopycnals near Lion. The 29.11 isopycnal is around 500 m depth (Fig. 10), and the 29.12 isopycnal is around 1600 m depth, locally up to 1300 m depth in IPSY. The doming is more centered around Lion in IPSY, whereas it is located more south-westward in IM36 (Figs. 10 and 11). During SOP2 (15 February), the formation of new dense water in surface has began in IM36, with the outcropping of the 29.11 density surface. In IPSY, DWF is very small at that date. It mostly amplifies around 25 February (IOP24).

On the contrary, IMAP shows an overestimation of the convection, with a large deep-convective patch extended eastward and more profiles showing mixed layer reaching the seafloor than observed (Fig. 9). In fact, IMAP contains few dense water before SOP2 ($\sim1\times10^5$ km^3 of water denser than 29.11 kg.m^{-3} in the north-western Mediterranean and no water denser than 29.12 kg.m^{-3} in January, Fig. 12). The strong wind events at the beginning of February (IOPs 21a and 21c) trigger the formation of dense water ($\sim$29.11 kg.m^{-3}) in surface over an elongated area from the Catalonian Sea to the Ligurian Sea (Fig. 10). It quasi immediately propagates deepwards thanks to the very low stratification.

For the three experiments, during IOP24, water denser than 29.12 kg.m^{-3} (and even reaching 29.13 kg.m^{-3}) is formed (Fig. 11 and 12). Then, a period of restratification occurs. Finally, the end of SOP2 (15 March) is a period of new formation of dense water, denser than 29.12 kg.m^{-3}. At the same time, the dense water, just formed during the previous month, begins to propagate deepwards and south-westwards (Fig. 10 and 11).

7. Discussions and Conclusion

This study investigates the DWF representation in three sensitivity experiments with the NEMO-WMED36 ocean model, using different initial and boundary conditions. Three different datasets were used: outputs of the MED36 regional ocean model, analyses from the PSY2 operational system, and a mixed re-analysed/analysed product (MOOSE-ASICS/PSY2). But, the same high-resolution (2.5 km) high-frequency (1 h) atmospheric forcing is used, given by the AROME-WMED operational forecasts. This forcing well represents the meteorological conditions during SOP2. The air-sea fluxes forecasted by AROME-WMED show the large heat and water losses for the ocean during SOP2, with integrated values (over one month and a half) corresponding to approximately -1000 PJ by squared kilometer (for heat) and 200 millions of tons of water loss by squared kilometer in the GoL. However, the biases in the meteorological parameters, in the AROME-WMED SST field, as the uncertainties linked to the turbulent flux parameterization, can lead to errors in the flux values we can not verify as no direct observation of surface turbulent fluxes are available during the strong wind events of HyMeX-SOP2. In particular, the sensible heat loss is probably overestimated by ECUME during mistral events, as already shown by *Rainaud et al.* [2015]. Large uncertainties also exist for the radiative heat fluxes and precipitation over sea. Nevertheless, the comparison against moored buoy observations and the evaluation of the simulated ocean evolution tend to prove the generally good quality of the high-resolution hourly forcing produced by AROME-WMED short-range forecasts.

The main conclusion of this sensitivity study is that the DWF simulation depends strongly on the initial conditions and in particular of the stratification index. To represent

the stratification at the beginning of winter, we calculate IS averaged on a $1° \times 1°$ box around the Lion buoy, on January 15, just before the deep convection occurs. IM36 is filled by dense water before SOP2 and has an IS of 0.39 $m^2.s^{-2}$ the 15 January, which delays the deep convection.

On the contrary, IMAP shows a very low stratification ($IS_{15jan} = 0.24\ m^2.s^{-2}$). The deep convection occurs sooner, over a very large area (74297 km^2) in the north-western Mediterranean Sea, and with a huge amount of new 29.11 kg.m^{-3} water formed during SOP2 (∼2.6 Sv, Tab. 3). IPSY has the strongest stratification ($IS_{15jan} = 0.47\ m^2.s^{-2}$) and presents the smallest convective area (26936 km^2), 3 times less than IMAP, with an underestimation compared to in-situ density profiles.

A summary of the water characteristics in the north-western Mediterranean region for the three experiments is shown in Figure 13. It confirms the very large differences found in surface (AW) characteristics and in terms of stratification (LIW barrier). For WMDW, Argo floats show water of σ=29.118 kg.m^{-3} (θ=12.9 °C and S=38.485 psu) at ∼2000 m depth. IMAP has thus the best performances in terms of WMDW θ/S characteristics (θ=12.92 °C and S=38.485 psu). IPSY dense waters are a little too salty (S=38.497 psu) and IM36 has too cold and fresh WMDW (θ=12.79 °C and S=38.455 psu).

The estimation of the dense water formation rate in the north-western Mediterranean Sea during SOP2 is still challenging. An estimation using four successive CTD campaigns in the area gives a production of water denser than 29.11 kg.m^{-3} for winter 2013 of 1.84±0.48 Sv [*Waldman et al.*, 2016]. The simulated DWF rates computed for SOP2 in Table 3 show that IPSY produces few new dense water (∼0.6 Sv of water denser than 29.11 kg.m^{-3} and 0.3 Sv of water denser than 29.12 kg.m^{-3}). IM36 shows a larger production

of the most dense water (∼1 Sv of water denser than 29.11 kg.m^{-3} and 0.84 Sv of water denser than 29.12 kg.m^{-3}). But, IMAP shows the largest production (∼2.6 Sv of water denser than 29.11 kg.m^{-3}) in coherence with a too large simulated convection itself favored by a very low stratification in the MOOSE-ASICS analysis.

Note, however, that these estimations of the DWF rates should be temperated. Indeed, the simulations presented here end on 15 March 2013, because of the stop of the AROME-WMED operational system at the end of HyMeX-SOP2. As a consequence, our study could miss a part of the winter convection event. Nevertheless, the Lion buoy observations do not show the occurrence of strong mistral events after this date (not shown), indicating that IOP28 is the surely the last convective event. In addition, the convection in NEMO-WMED36 is parameterized with an enhanced vertical diffusion which is set to the constant large value 10 $m^2.s^{-1}$. Even if this convection parameterization is very often used, it is an inaccurate representation of convection because the vertical diffusion is a local mixing while convection is a non-local mixing. In particular for high-resolution modelling systems which represent fine-scale sctructures and thus very strong stratification gradients this rough representation of convection is unappropriated. In regions where the stratification is unstable, such enhanced coefficient is usually tuned to minimize the simulation discrepancies because the vertical diffusion is not designed to represent convective transports. Large differences in IS were observed between IMAP, IM36 and IPSY simulations which used identical and constant enhanced vertical diffusivity coefficient. This coefficient is probably not adapted for IMAP, which used low stratified initial conditions compared to others, because the convection area is too large. This result highlights the limitations of rough parameterization of convection which needs to be significantly

improved in the future. This important issue for DWF is addressed in the ASICS-Med project.

Moreover, within the framework of this same project, the next step of this study is to evaluate the high-resolution air-sea coupled processes impact on DWF, using the NEMO-AROME WMED coupled system [*Lebeaupin Brossier et al.*, 2016]. We particularly aim at investigating the sea surface (temperature and (sub)mesoscale circulation features) role on the air-sea fluxes and their feedback on DWF.

Notations

Models and parameterizations

AROME	Application of Research to Operations at MEsoscale
AROME-WMED	Western Mediterranean configuration of AROME
ARPERA	ERA40 dynamical downscaling by ARPEGE-Climate
NEMO	Nucleus for European Modelling of the Ocean
(NEMO-)MED36	Mediterranean basin configuration of NEMO (1/36°-resolution)
(NEMO-)WMED36	Western Mediterranean basin configuration of NEMO (1/36°-resolution)
PSY2(V4R4)	Regional operational NEMO configuration from Mercator Océan (1/12°-resolution)
RRTM	Rapid Radiative Transfert Model
SURFEX	Surface Externalized
TVD	Total Variance Dissipation scheme

NEMO-WMED36 simulations

IM36	initialization with MED36
IMAP	initialization with the MOOSE-ASICS analysis and PSY2
IPSY	initialization with PSY2

Fields and constants

DD10	10 m wind direction
E	Evaporation
F	Freshwater flux
FF10	10 m wind velocity
H	Sensible heat flux
IS	Index of Stratification
$\mathcal{L}$	Latent heat of vaporization
LE	Latent heat flux
LW	Long-wave radiative flux
MLD	Mixed Layer Depth
N	Brunt-Väisälä frequency
P	Precipitation
Q	Net heat flux
S	Salinity
R_d	Rossby deformation radius
RH2M	2 m relative humidity
SSS	Sea Surface Salinity
SST	Sea Surface Temperature
SW	Short-wave-radiative flux
θ	Potential ocean temperature
τ, τ_u, τ_v	Wind stress and components
T2M	2 m air temperature
U	zonal ocean velocity
V	meridional ocean velocity

Observations

CTD	Conductivity Temperature Depth
IOP	Intensive Observations Period
P/T	Port-Tender
SOP	Special Observations Period
R/V	Research-Vessel
XBT	eXpendable BathyThermograph

Water masses, processes and locations

AW	Atlantic Water
DWF	Dense Water Formation
GoL	Gulf of Lion
LIW	Levantine Intermediate Water
WIW	Western *(Winter)* Intermediate Water
WMDW	Western Mediterranean Dense Water

Projects

ASICS-Med	Air-Sea Interaction and Coupling with Submesoscale structures in the Mediterranean
HyMeX	Hydrological cycle in the Mediterranean Experiment
IODA-Med	Inovative Observing and Data Assimilation systems for severe weather events in the Mediterranean
MISTRALS	Mediterranean Integrated STudies at Regional And Local Scales
MOOSE	Mediterranean Ocean Observing System for the Environment
SiMed	Simulation of the Mediterranean Sea

Acknowledgments. This work is a contribution to the HyMeX program (*HYdrological cycle in the Mediterranean EXperiment* - www.hymex.org) through INSU-MISTRALS support, through SiMed (*SImulation of the MEDiterranean Sea*) transverse axe support and through the ASICS-MED project (*Air-Sea Interaction and Coupling with Submesoscale structures in the MEDiterranean*, ANR-2012-BS06-003). The authors acknowledge Météo-France for supplying the AROME-WMED operational forecasts, sponsored by Grants MISTRALS/HyMeX and IODA-MED project (*Inovative Observing and Data Assimilation systems for severe weather events in the MEDiterranean*, ANR-11-BS56-0005), and the two moored buoys dataset. The authors also acknowledge Mercator Océan for supplying the PSY2V4R4 analysis and the HyMeX database teams (ESPRI/IPSL and SEDOO/OMP) for their help in accessing the data. The authors gratefully thank the Principal Investigators of the MOOSE-GE and DeWEX cruises [L. Coppola (LOV), L. Mortier and P. Testor (LOCEAN)] and of the R/V *Téthys II* and P/T *Le Provence* cruises during HyMeX-SOP2 [I. Taupier Letage (MIO)]. Finally, the authors thank the two anonymous reviewers who helped to improve this manuscript. The Argo floats, gliders and CTD profiles dataset were collected and made freely available by the Coriolis project and programmes that contribute to it (http://www.coriolis.eu.org).

References

Adloff, F., S. Somot, F. Sevault, G. Jordà, R. Aznar, M. Déqué, M. Herrmann, M. Marcos, C. Dubois, E. Padorno, E. Alvarez-Fanjul, and D. Gomis, (2015), Mediterranean Sea response to climate change in an ensemble of twenty first century scenarios. *Clim. Dyn.*, *45 (9)*, 2775-2802, doi:10.1007/s00382-015-2507-3.

Arsouze, T., J. Beuvier, K. Béranger, S. Somot, C. Lebeaupin Brossier, R. Bourdallé-Badie, F. Sevault, Y. Drillet (2013), Sensibility analysis of the Western Mediterranean Transition inferred by four companion simulations, *Proceedings of CIESM Congress*, November 2013, Marseille, France.

Belamari, S. (2005), Report on uncertainty estimates of an optimal bulk formulation for turbulent fluxes. *MERSEA IP Deliverable*, *D.4.1.2*, 31pp

Belamari, S. and A. Pirani (2007), Validation of the optimal heat and momentum fluxes using the ORCA-LIM global ocean-ice model. *MERSEA IP Deliverable*, *D.4.1.3*, 88pp.

Barnier, B., G., Madec, T., Penduff, J.-M., Molines, A.-M., Tréguier, J., Le Sommer, A., Beckmann, A., Biastoch, C., Böning, J., Dengg, C., Derval, E., Durand, S., Gulev, E., Rémy, C., Talandier, S., Theetten, M.E., Maltrud, J., McClean, and B., De Cuevas, (2006), Impact of partial steps and momentum advection schemes in a global ocean circulation model at eddy-permitting resolution, *Ocean Dyn.*, *56*(5-6), 543-567, doi: 10.1007/s10236-006-0082-1.

Béranger, K., Y. Driller, M-N. Houssais, P. Testor, R. Bourdallé-Badie, B. Alhammoud, A. Bozec, L. Mortier, P. Bouruet-Aubertot and M. Crépon (2010), Impact of the spatial distribution of the atmospheric forcing on water mass formation in the Mediterranean Sea, *J. Geophys. Res.*, *115*, C12041, doi:10.1029/2009JC005648.

Beuvier, J., F. Sevault, M. Herrmann, H. Kontoyiannis, W. Ludwig, M. Rixen, E. Stanev, K. Béranger, S. Somot (2010), Modelling the Mediterranean Sea interannual variability during 1961-2000: Focus on the Eastern Mediterranean Transient (EMT), *J. Geophys. Res.*, *115* C08517, doi:10.1029/2009JC005950.

Beuvier, J., K. Béranger, C. Lebeaupin Brossier, S. Somot, F. Sevault, Y. Drillet, R. Bourdallé-Badie, N. Ferry, B. Levier, and F. Lyard (2012), Spreading of the Western Mediterranean Deep Water after winter 2005: time-scales and deep cyclone transport. *J. Geophys. Res.*, *117*, C07022, doi:10.1029/2011JC007679.

Blanke, B., and P. Delecluse, (1993), Variability of the tropical Atlantic ocean simulated by a general circulation model with two different mixed layer physics, *J. Phys. Oceanogr*, *23*, 1363-1388.

Canals, M., P. Puig, X. Durrieu de Madron, S. Heussner, A. Palanques, and J. Fabres (2006), Flushing submarine canyons, *Nature*, *444*, 354-357.

Castellari, S. N. Pinardi, K. Leaman (2000), Simulation of the water mass formation processes in the Mediterranean Sea: Influence of the time frequency of the atmospheric forcing, *J. Geophys. Res.*, *105*, 24157-24181, doi:10.1029/2000JC900055.

De Mey, P., and P. Ménard (1989), Synoptic analysis and dynamical adjustment of GEOS 3 and Seasat altimeter eddy fields in the northwest Atlantic, *J. Geophys. Res.*, *94*(C5), 6221-6230, doi:10.1029/JC094iC05p06221.

Drobinski, P., V. Ducrocq, P. Alpert, E. Anagnostou, K. Béranger, M. Borga, I. Braud, A. Chanzy, S. Davolio, G. Delrieu, C. Estournel, N. Filali Boubrahmi, J. Font, V. Grubisic, S. Gualdi, V. Homar, B. Ivancan-Picek, C. Kottmeier, V. Kotroni, K. Lagouvardos, P. Lionello, M. C. Llasat, W. Ludwig, C. Lutoff, A. Mariotti, E. Richard, R. Romera, R.

Rotunno, O. Roussot, I. Ruin, S. Somot, I. Taupier-Letage, J. Tintore, R. Uijlenhoet, H. Wernli (2014), HyMeX, a 10-year multidisciplinary program on the Mediterranean water cycle, *BAMS*, *95*, 1063-1082, doi:10.1175/BAMS-D-12-00242.1.

Ducrocq, V., I. Braud, S. Davolio, R. Ferretti, C. Flamant, A. Jansa, N. Kalthoff, E. Richard, I. Taupier-Letage, P-A. Ayral, S. Belamari, A. Berne, M. Borga, B. Boudevillain, O. Bock, J-L. Boichard, M-N. Bouin, O. Bousquet, C. Bouvier, J. Chiggiato, D. Cimini, U. Corsmeier, L. Coppola, P. Coquerez, E. Defer, J. Delanoe, P Di Girolamo, A. Doerenbecher, P. Drobinski, Y. Dufournet, N. Fourrié, J. J. Gourley, L. Labatut, D. Lambert, J. Le Coz, F. S. Marzano, G. Molinié, A. Montani, G. Nord, M. Nuret, K. Ramage, B. Rison, O. Roussot, F. Said, A. Schwarzenboeck, P. Testor, J. Van Baelen, B. Vincendon, M. Aran, J. Tamayo, 2014: HyMeX-SOP1, the field campaign dedicated to heavy precipitation and flash flooding in the northwestern Mediterranean. *Bull. Amer. Meteorol. Soc.*, *95*, 1083-1100, doi:10.1175/BAMS-D-12-00244.1.

Dufau-Julliand, C., P. Marsaleix, A. Petrenko, I. Dekeyser (2004), Three-dimensional modeling of the Gulf of Lions hydrodynamics (northwest Mediterranean) during January 1999 (MOOGLI3 Experiment) and late winter 1999: Western Mediterranean Intermediate Waters (WIWs) formation and cascading over the shelf break. *J. Geophys. Res.*, *109*, C11002. doi:10.1029/2003JC002019.

Estournel, C., P. Broch, P. Marsaleix, J-L. Devenon, F. Auclair, R. Vehil (2001): The Rhône river plume in unsteady conditions: numerical and experimental results. *Estuarine Coastal Shelf Sci.*, *53*, 25-38.

Estournel, C., P. Testor, I. Taupier-Letage, M-N. Bouin, L. Coppola, P. Durand, P. Conan, L. Beguery, S. Belamari, K. Béranger, J. Beuvier, D. Bourras, G. Canut, A. Doeren-

becher, P. Drobinski, V. Ducrocq, H. Giordani, D. Hauser, L. Labatut, C. Lebeaupin Brossier, M. Nuret, L. Prieur, O. Roussot, S. Somot, (2016 rev.), HyMeX-SOP2, the field campaign dedicated to dense water formation in the northwestern Mediterranean, *Oceanography*.

Flamant, C. (2003), Alpine lee cyclogenesis influence on air-sea heat exchanges and marine atmospheric boundary layer thermodynamics over the western Mediterranean during a Tramontane/Mistral event. *J. Geophys. Res.*, *108*(C2), 8057, doi: 10.1029/2001JC001040.

Fouquart, Y. and B. Bonnel (1980), Computations of solar heating of the earth's atmosphere: A new parameterization. *Beitr. Phys. Atmos.*, *53*, 35-62.

Fourrié, N., É. Bresson, M. Nuret, C. Jany, P. Brousseau, A. Doerenbecher, M. Kreitz, O. Nuissier, E. Sevault, H. Bénichou, M. Amodei, and F. Pouponneau (2015): AROME-WMED, a real-time mesoscale model designed for HyMeX Special Observation Periods. *Geosci. Model. Dev.*, *8*, 1919-1941, doi:10.5194/gmd-8-1919-2015.

Gasparini, G., P., G. Zodiatis, M. Astraldi, C. Galli, S. Sparnocchia (1999), Winter intermediate water lenses in the Ligurian Sea. *J. Mar. Syst.*, *20*(1-4), 319-332.

Giordani, H., G. Caniaux, L. Prieur, A. Paci, S. Giraud (2005), A 1 year mesoscale simulation of the northeast Atlantic: Mixed layer heat and mass budgets during the POMME experiment. *J. Geophys. Res.*, *110*(C07S08), doi:10.1029/2004JC002765.

Herrmann, M., and S. Somot (2008), Relevance of ERA40 dynamical downscaling for modeling deep convection in the Mediterranean Sea. *Geophys. Res. Lett.*, *35*, L04607, doi:10.1029/2007GL032442.

Jackett, D. R. and T. J. McDougall (1994), Minimal adjustment of hydrographic profiles to achieve static stability. *J. Atmos. Ocean Tech.*, *12*, 381-389.

Juza, M., L. Renault, S. Ruiz, and J. Tintoré (2013), Origin and pathways of Winter Intermediate Water in the Northwestern Mediterranean Sea using observations and numerical simulation, *J. Geophys. Res.*, *118*, 6621-6633, doi:10.1002/2013JC009231.

Lazar, A., G. Madec, P. Delecluse, (1999), The deep interior downwelling in the Veronis effect, and mesoscale tracer transport parameterizations in an OGCM. *J. Phys. Oceanogr.*, *29*, 2945-2961.

Lebeaupin Brossier, C., and P. Drobinski (2009), Numerical high-resolution air-sea coupling over the Gulf of Lions during two Tramontane/Mistral events. *J. Geophys. Res.*, *114*, D10110, doi:10.1029/2008JD011601.

Lebeaupin Brossier, C., K. Béranger, and P. Drobinski (2012), Sensitivity of the northwestern Mediterranean Sea coastal and thermohaline circulations simulated by the 1/12°-resolution ocean model NEMO-MED12 to the spatial and temporal resolution of atmospheric forcing, *Ocean Modelling*, *43-44*, 94-107.

Lebeaupin Brossier, C., T. Arsouze, K. Béranger, M-N. Bouin, É. Bresson, V. Ducrocq, H. Giordani, M. Nuret, R. Rainaud, I. Taupier-Letage (2014), Ocean mixed layer responses to intense meteorological events during HyMeX-SOP1 from a high-resolution ocean simulation. *Ocean Modelling*, *84*, 84-103, doi:10.1016/j.ocemod.2014.09.009.

Lebeaupin Brossier, C., F. Léger, H. Giordani, J. Beuvier, M-N. Bouin, V. Ducrocq, N. Fourrié (2016 sub.), Dense Water Formation in the North-Western Mediterranean area during HyMeX-SOP2 in 1/36° ocean simulations: Ocean-atmosphere coupling impact. *J. Geophys Res.*

Lellouche, J-M., O. Le Galloudec, M. Drévillon, C. Régnier, E. Greiner, G. Garric, N. Ferry, C. Desportes, C-E. Testut, C. Bricaud, R. Bourdallé-Badie, B. Tranchant, M. Benkiran, Y. Drillet, A. Daudin, C. De Nicola (2013), Evaluation of global monitoring and forecasting systems at Mercator Océan. *Ocean Sci.*, *9*, *57-81*, doi:10.5194/os-9-57-2013.

Lyard, F., F. Lefevre, T. Letellier, and O. Francis (2006), Modelling the global ocean tides: modern insights from FES2004, *Ocean Dynamics*, *56* (5-6), 394-415.

Madec, G., M. Chartier, P. Delecluse, M. Crépon (1991), A three-dimensional numerical studies of Deep-Water Formation in the Northwestern Mediterranean Sea. *J. Phys. Oceanogr.*, *21*, 1349-1371.

Madec, G. (2008), NEMO ocean engine, *Note du Pole de modélisation, Institut Pierre-Simon Laplace (IPSL), France*, No 27 ISSN No 1288-1619.

Marshall, J., and F. Schott (1999), Open-ocean convection: Observations, theory, and models, *Reviews of Geophysics*, *37* (1), 1-64.

Masson, V., P. Le Moigne, E. Martin, S. Faroux, A. Alias, R. Alkama, S. Belamari, A. Barbu, A. Boone, F. Bouyssel, P. Brousseau, E. Brun, J.-C. Calvet, D. Carrer, B. Decharme, C. Delire, S. Donier, K. Essaouini, A.-L. Gibelin, H. Giordani, F. Habets, M. Jidane, G. Kerdraon, E. Kourzeneva, M. Lafaysse, S. Lafont, C. Lebeaupin Brossier, A. Lemonsu, J.-F. Mahfouf, P. Marguinaud, M. Mokhtari, S. Morin, G. Pigeon, R. Salgado, Y. Seity, F. Taillefer, G. Tanguy, P. Tulet, B. Vincendon, V. Vionnet, and A. Voldoire (2013), The SURFEXv7.2 land and ocean surface platform for coupled and offline simulation of earth surface variables and fluxes. *Geosci. Model Dev.*, *6*, 929-960, doi:10.5194/gmd-6-929-2013.

MEDAR/MEDATLAS Group (2002), *MEDAR/MEDATLAS 2002 Database, Mediterranean and Black Sea database of temperature salinity and bio-chemical parameters*, Climatological Atlas, IFREMER Edition, Brest, France, 4 CDRom.

Mertens, C. and F. Schott (1998), Interannual variability of deep-water formation in the northwestern Mediterranean, *J. Phys. Oceanogr.*, *28*, 1410-1424.

Millot, C. (1979) Wind induced upwellings in the Gulf of Lions. *Oceanol. Acta*, *2*, 261-274.

Millot, C. (1982), *Analysis of upwelling in the Gulf of Lions*. In: Nihoul, J.C.J. (Ed.), Hydrodynamics of Semi-enclosed Seas: Proceeding of the 13th International, Lige Colloquium on Ocean Hydrodynamics, Elsevier Oceanography Series, vol. *34*. Elsevier Science Publishing, Amsterdam, The Netherland, pp. 143-153.

Millot, C. (1999), Circulation in the Western Mediterranean Sea. *J. Mar. Syst.*, *20* (14), 423-442.

Millot, C. and I. Taupier-Letage (2005), Circulation in the Mediterranean sea, In *The Mediterranean Sea*, pages 29-66. Springer.

Mlawer, E.J., S.J. Taubman, P.D. Brown, M.J. Iacono and S.A. Clough (1997), Radiative transfer for inhomogeneous atmospheres: RRTM, a validated correlated-k model for the longwave, *J. Geophys. Res.*, *102*, 16663-16682.

Ourmières, Y., B. Zakardjian, K. Béranger, C. Langlais (2011), Assessment of a NEMO-based downscaling experiment for the North-Western Mediterranean region: impacts on the Northern Current and comparison with ADCP data and altimetry products, *Ocean Model.*, *39* (34), 386-404.

Rainaud, R., C. Lebeaupin Brossier, V. Ducrocq, H. Giordani, M. Nuret, N. Fourrié, M.-N. Bouin, I. Taupier-Letage, D. Legain (2015): Characterisation of air-sea exchanges over

the Western Mediterranean Sea during the HyMeX SOP1 using the AROME-WMED model, *Q. J. R. Meteorol. Soc.*, doi:10.1002/qj.2480.

Roullet G. and G. Madec (2000), Salt conservation, free surface and varying levels: A new formulation for ocean general circulation models, *J. Geophys. Res.*, *105*(C10), 23927-23942, doi:10.1029/2000JC900089.

Schott, F., M. Visbec, U. Send, J. Fischer, L. Stramma, Y. Desaubies (1996), Observations of deep convection in the Gulf of Lion, Northern Mediterranean, during the winter of 1991/1992, *J. Phys. Oceanogr.*, *26*, 505-524.

Seity, Y., P. Brousseau, S. Malardel, G. Hello, P. Bénard, F. Bouttier, C. Lac, V. Masson (2011), The AROME-France convective scale operational model, *Mon. Wea. Rev.*, *139*, 976-991

Small, R. J., S. Carniel, T. Campbell, J. Teixeira, R. Allard (2012), The response of the Ligurian and Tyrrhenian Seas to a summer mistral event: a coupled atmosphere-ocean approach, *Ocean Modelling*, *48*, 30-44.

Waldman, R., S. Somot, M. Herrmann, P. Testor, C. Estournel, F. Sevault, P. Conan, L. Coppola, D. Dausse, V. Taillandier, L. Prieur, L. Mortier (2016 rev.), Estimating dense water formation rates with an Observing System Simulation Experiment (OSSE): case study in the Northwestern Mediterranean sea. *J. Geophys Res.*

Zecchetto, S., F. De Biaso (2007), Sea surface winds over the Mediterranean Basin from satellite data (2000-04): meso- and local-scale features on annual and seasonal time scales, *J. Appl. Meteorol. Climato.*, *46*, 814-827.

Table 1. Numerical experiments. IC stands for initial conditions, BC for boundary conditions and SURF stands for surface atmospheric forcing.

Name	BEGIN	SPIN-UP	END	IC	BC	SURF
IM36	15 August 2012	yes 15 days	15 March 2013	MED36 August 2012 (monthly)	MED36 (monthly)	AROME-WMED (2.5km, 1h)
IPSY	1 September 2012	no	15 March 2013	PSY2 1 September 2012	PSY2 (monthly)	AROME-WMED (2.5km, 1h)
IMAP	1 September 2012	no	15 March 2013	MOOSE-ASICS + PSY2 *Summer 2012*	PSY2 (monthly)	AROME-WMED (2.5km, 1h)

Table 2. Characteristics at the Lion buoy of the Intensive Observing Periods (IOPs) related to strong wind events.

	begin	end	max FF10 ($m.s^{-1}$)	mean DD10	min T2M (°C)
IOP21a	02-Feb-2013	04-Feb-2013	22.1	NW	6.8
IOP21c	06-Feb-2013	08-Feb-2013	21.1	NW	7.1
IOP21d	09-Feb-2013	11-Feb-2013	17.0	NNW	5.4
IOP22a	12-Feb-2013	15-Feb-2013	18.5	NW	8.7
IOP22d	15-Feb-2013	16-Feb-2013	14.4	NW	9.2
IOP24	23-Feb-2013	26-Feb-2013	20.1	WNW	3.1
IOP25	01-Mar-2013	03-Mar-2013	15.4	NE	9.7
IOP26	04-Mar-2013	07-Mar-2013	18.0	ESE	11.7
IOP28	13-Mar-2013	15-Mar-2013	23.2	NW	5.3

Table 3. Dense water formation rates (Sverdrup) in the three sensitivity experiment IM36, IPSY and IMAP. The DWF rate is calculated as the sum of all the increasing phases in the dense water volume time-serie (Fig. 12) divided by 1 year to obtain Sverdrups.

	DWF rates (Sv)			
	> 29.10 kg.m^{-3}	> 29.11 kg.m^{-3}	> 29.12 kg.m^{-3}	> 29.13 kg.m^{-3}
IM36	0.47	1.02	0.84	2.0×10^{-3}
IPSY	0.50	0.59	0.30	0.2×10^{-3}
IMAP	1.41	2.59	0.77	2.7×10^{-3}

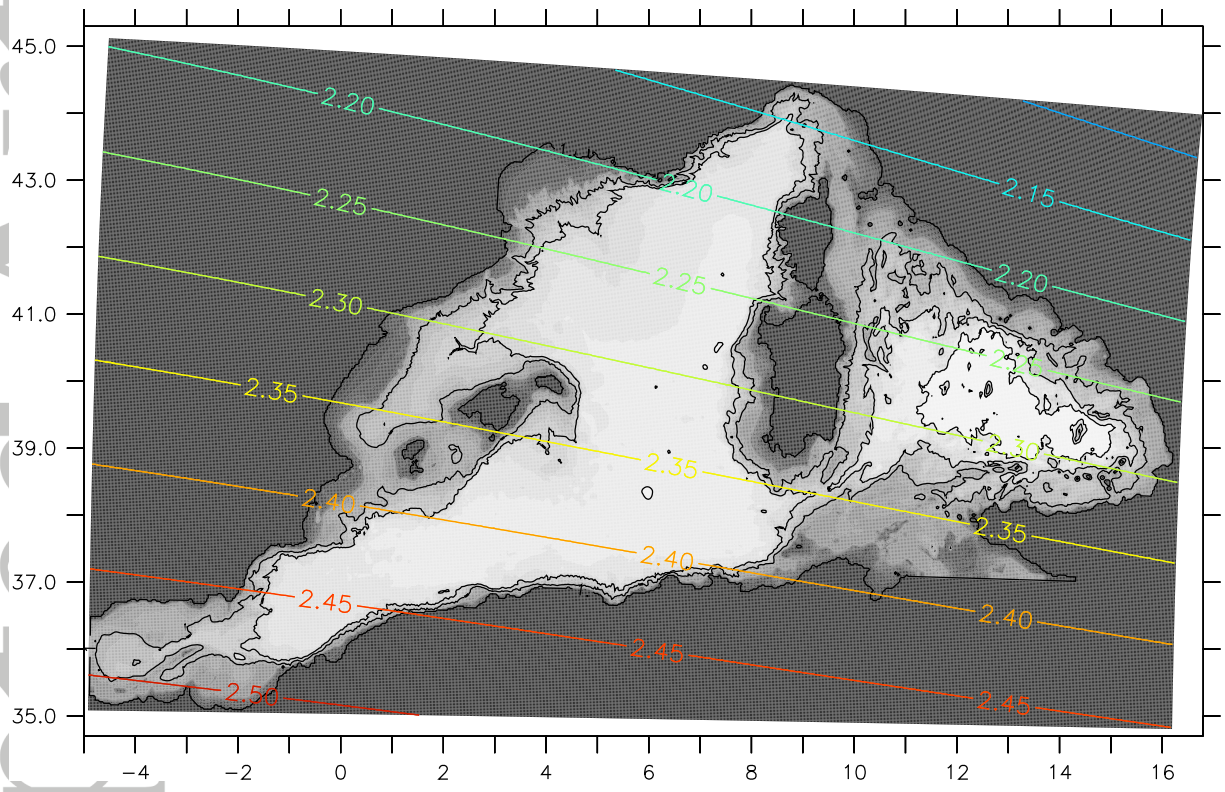

Figure 1. The NEMO-WMED36 domain illustrated by its bathymetry (grey shaded areas with black contours every 1000 m). The colored contours indicate the grid-mesh resolution (in kilometers).

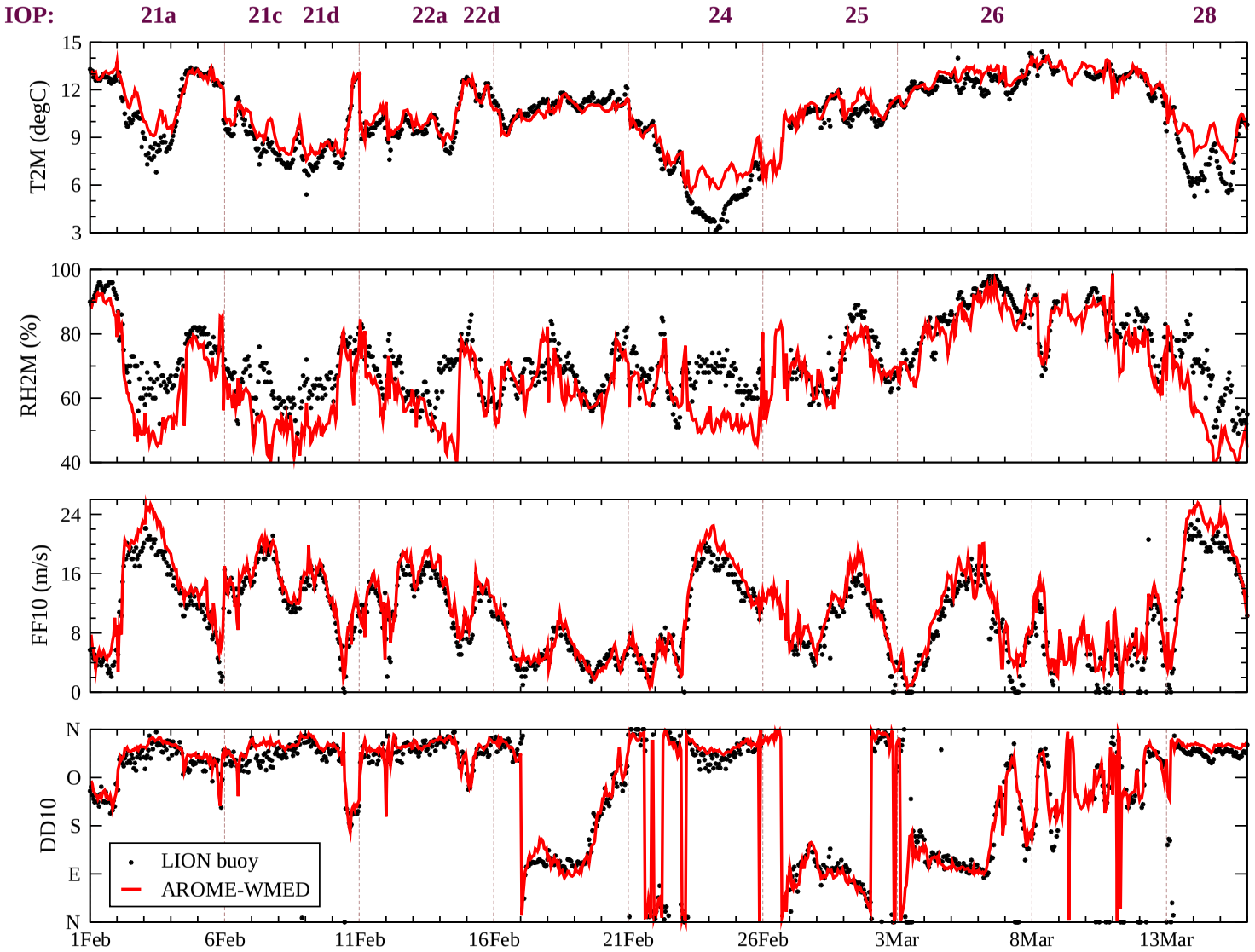

Figure 2. Time-series during SOP2 at the LION buoy (4.7°E-42.1°N) for 2m-temperature (T2M, °C), 2m-relative humidity (RH2M, %), 10m-wind speed (FF10, m.s^{-1}) and direction (DD10).

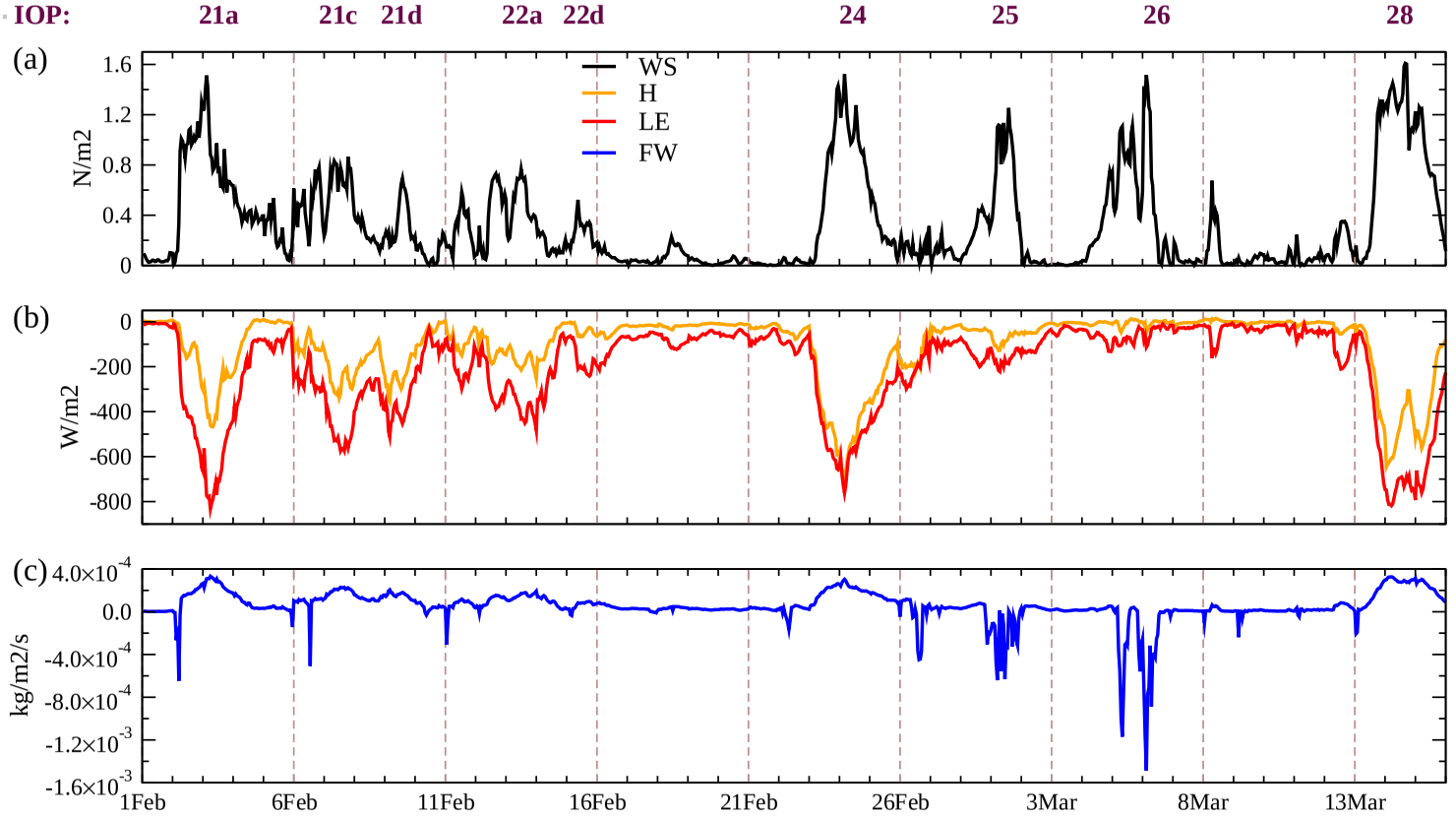

Figure 3. Time-series of air-sea fluxes during SOP2 at the LION buoy in AROME-WMED forecast: (a) wind stress (WS, $N.m^{-2}$), (b) sensible and latent heat fluxes (H and LE, $W.m^{-2}$, negative for ocean heat loss), and (c) fresh water flux (FW=E-P, $kg.m^{-2}.s^{-1}$).

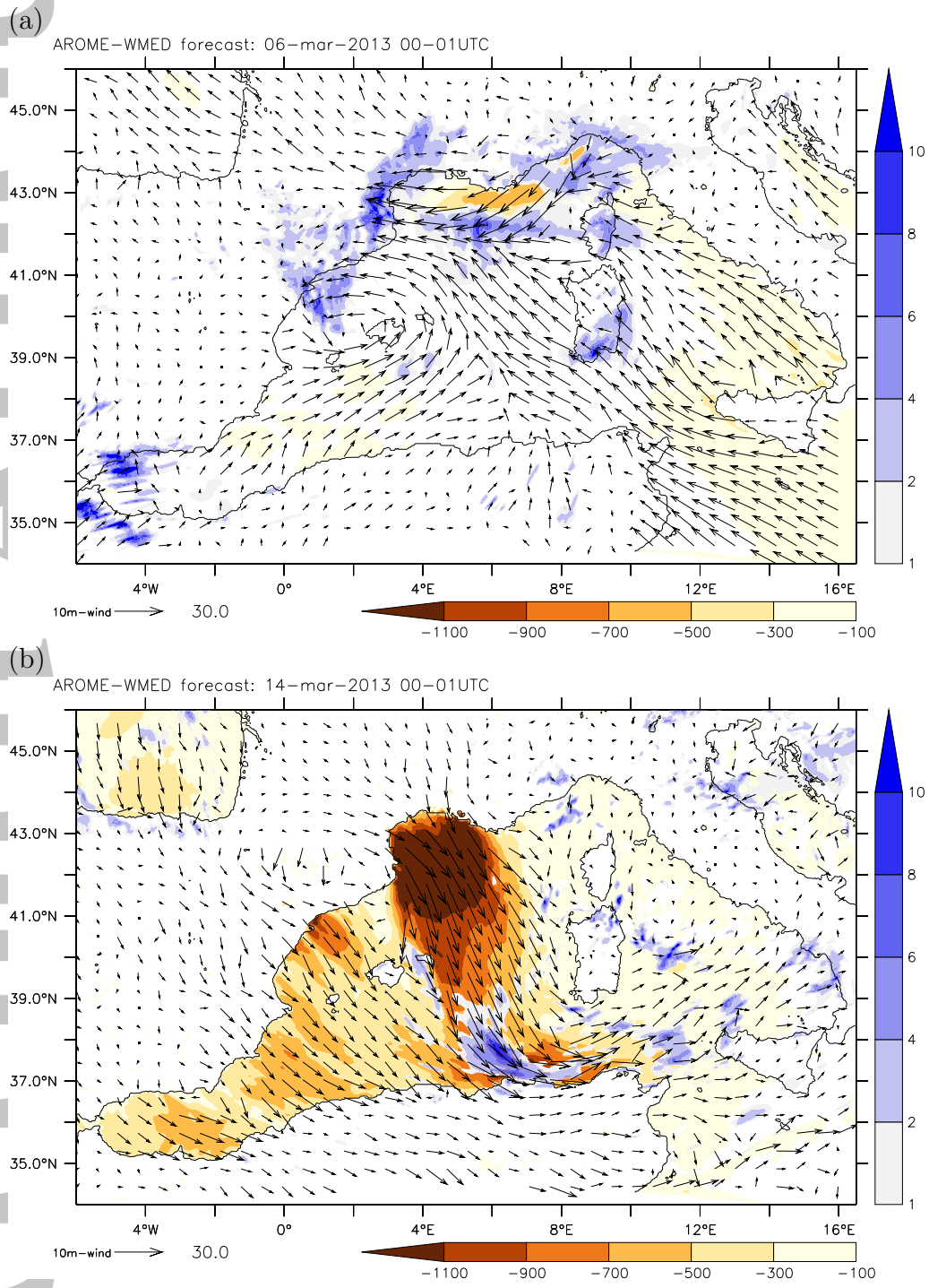

Figure 4. AROME-WMED forecast for (a) IOP26 (6 March 2013 01 UTC) and (b) IOP28 (14 March 2013 01 UTC): sea surface net heat flux (W.m^{-2}, orange colors), hourly precipitation (mm, blue colors) and 10 m wind (m.s^{-1}, arrows).

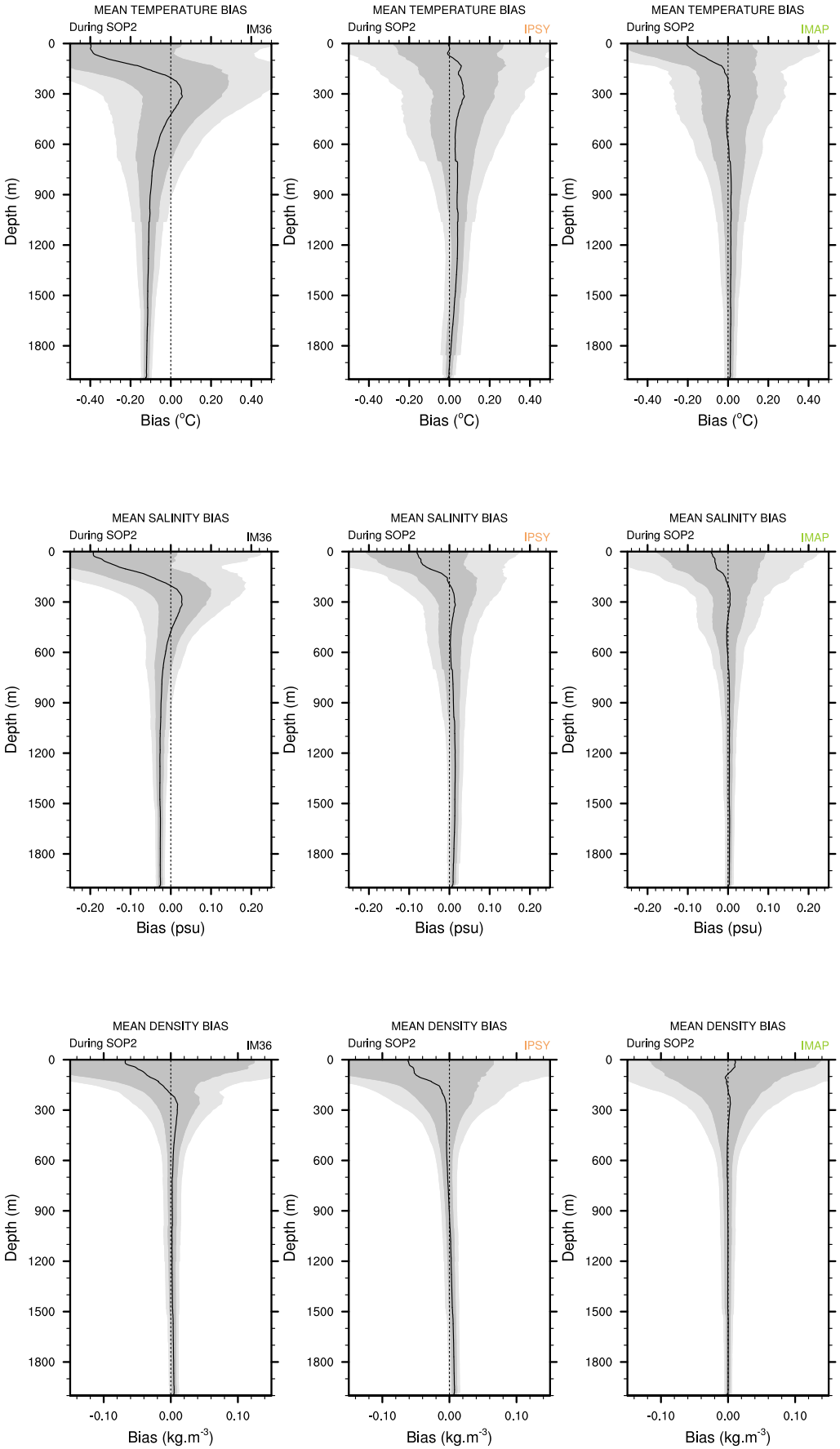

Figure 5. Mean vertical biases in temperature (°C), salinity (psu) and density (kg.m^{-3}) against the ARGO dataset of the whole SOP2, for the three experiment IM36, IPSY and IMAP. The darkgrey area is $\pm\sigma$; the lightgrey area is for $\pm 2\sigma$.

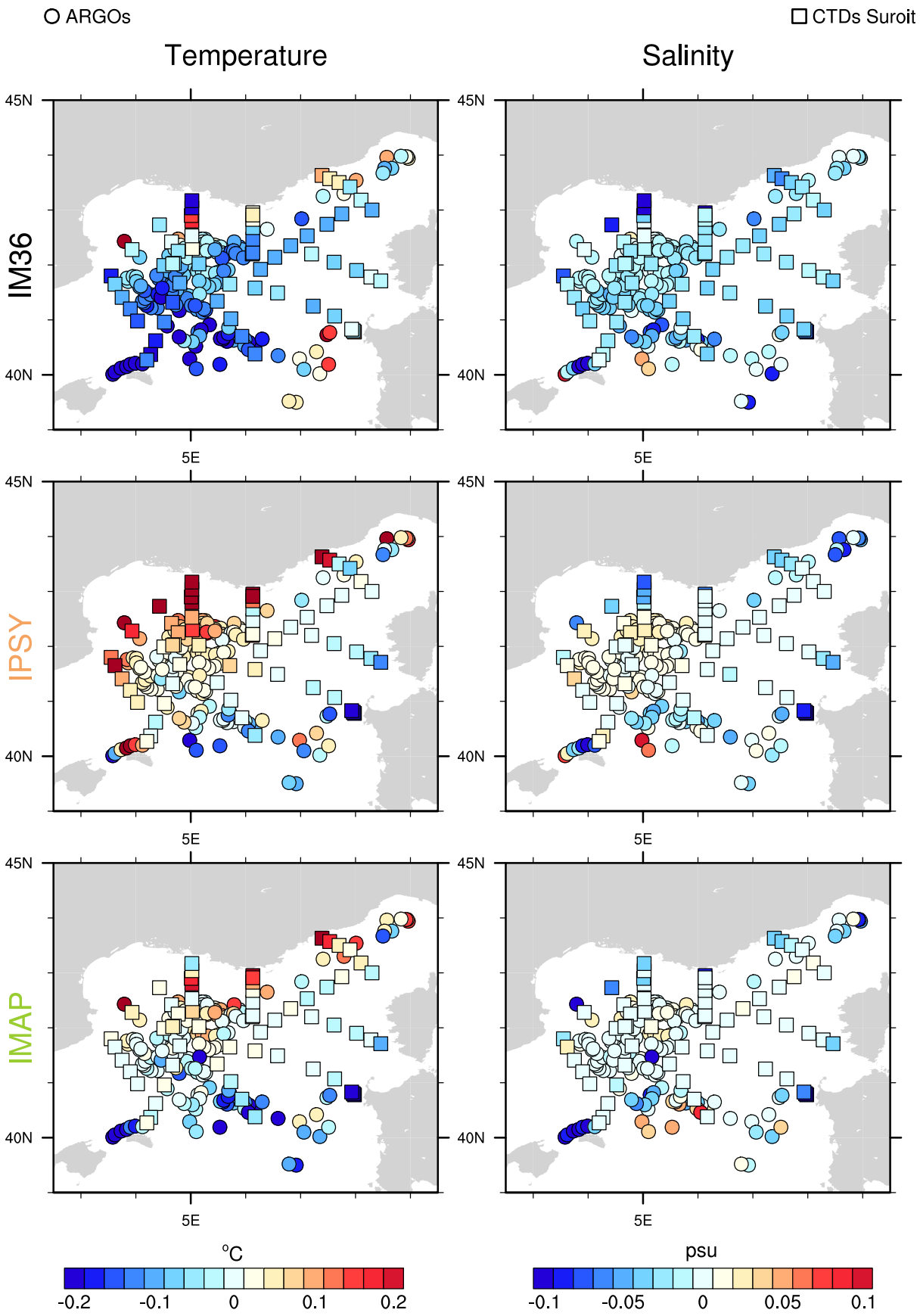

Figure 6. Vertically-averaged biases for temperature (left panels, °C) and salinity (right panels, psu) against in-situ profiles (ARGOs and *R/V Le Suroît* CTDs) for IM36 (top panels), IPSY (middle panels) and IMAP (bottom panels).

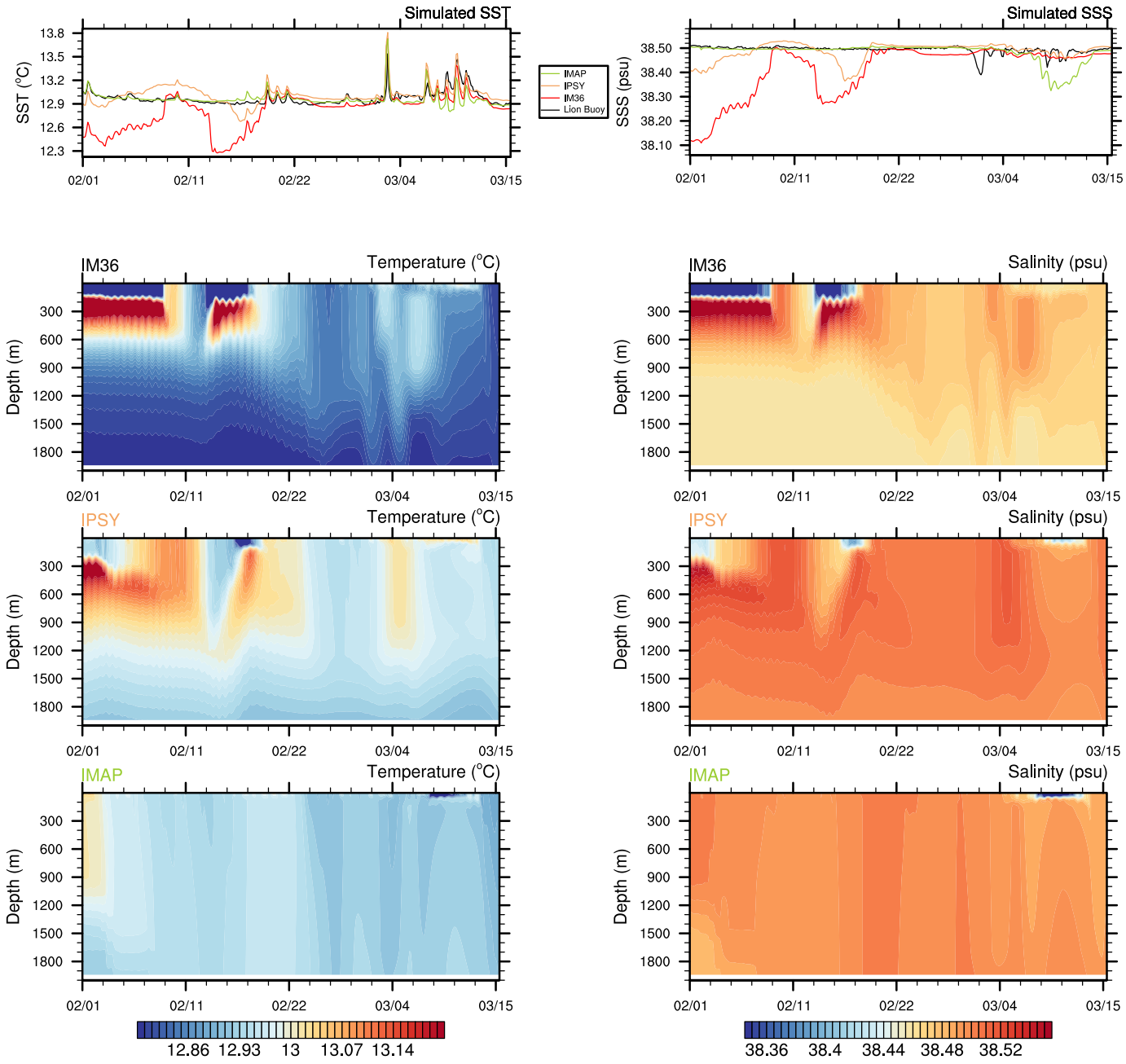

Figure 7. Lion buoy: Simulated and observed Sea Surface Temperature (SST, °C) and Salinity (SSS, psu) time-series. Temperature and salinity profiles hovmuller diagrams simulated by IM36, IPSY and IMAP.

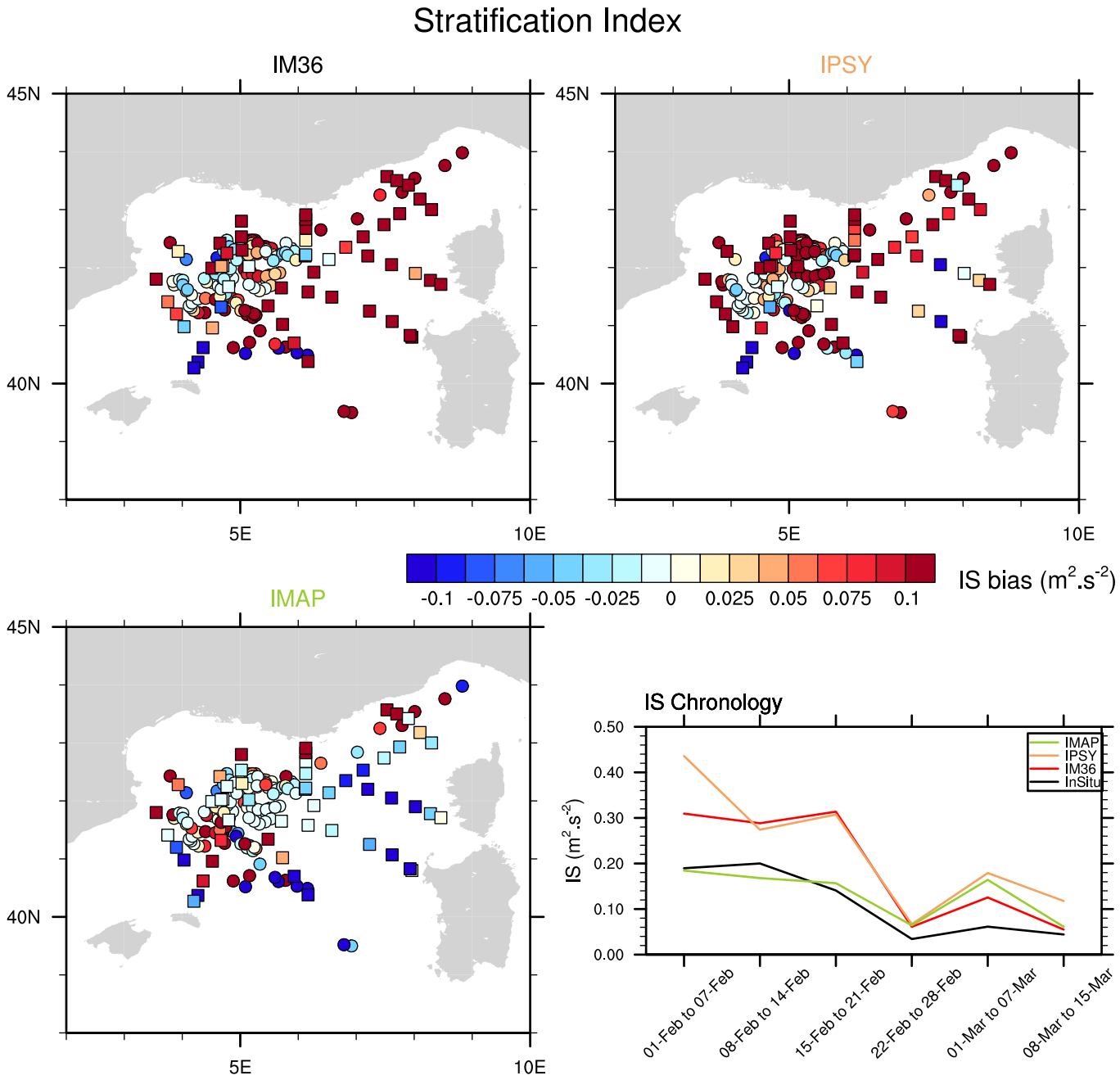

Figure 8. Index of Stratification (IS) biases ($m^2.s^{-2}$) against in-situ profiles (ARGOs and *R/V Le Suroît* CTDs) for IM36 (top left panel), IPSY (top right panel) and IMAP (bottom left panel). Bottom right panel: observed and simulated IS time-series during SOP2.

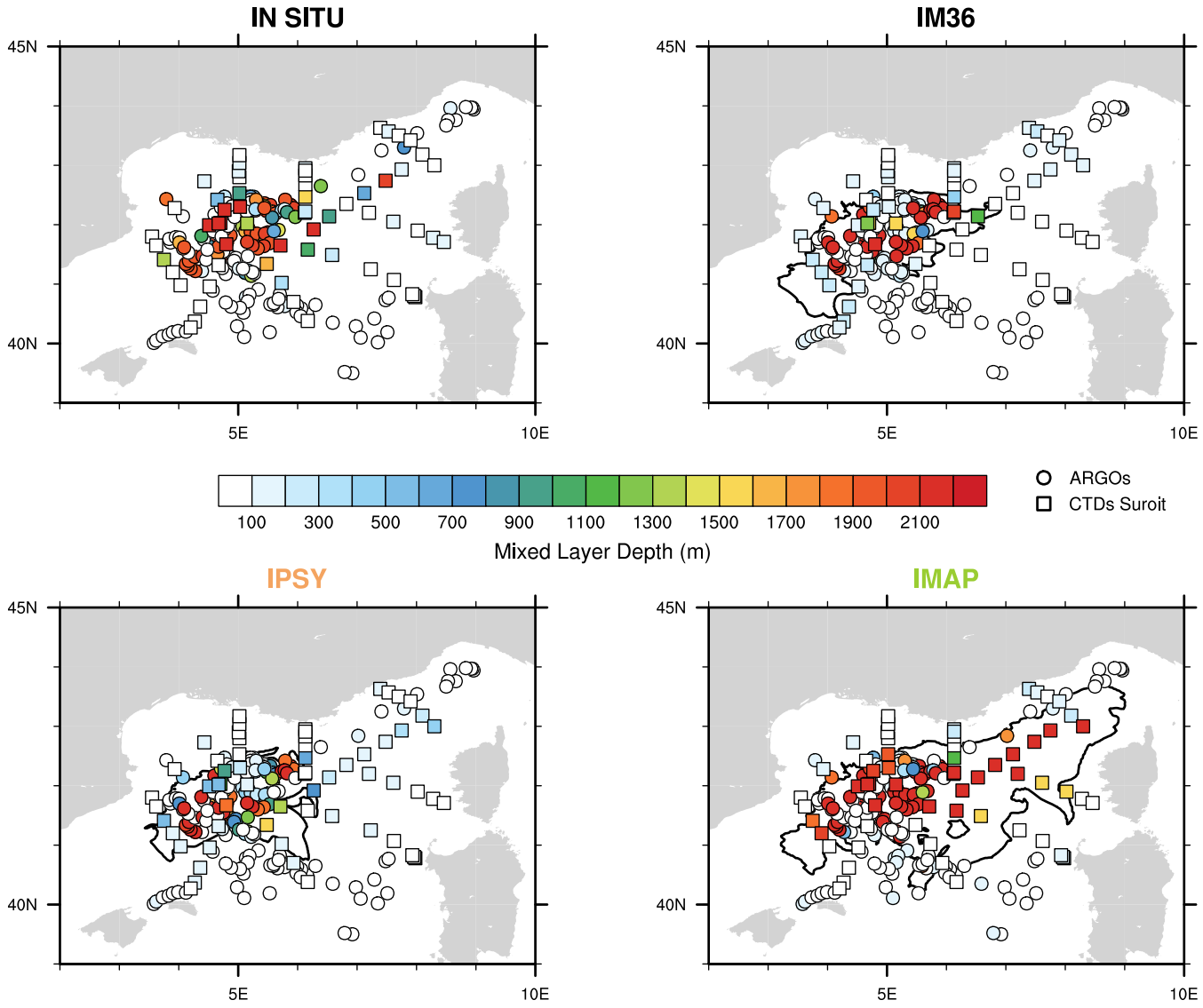

Figure 9. Mixed layer depth (meters) from density in-situ profiles (ARGOs and *R/V Le Suroît* CTDs) and colocalized simulated MLD (density criteria) in IM36, IPSY and IMAP. Contours indicate area where the maximum MLD goes deeper than 2000 meters during SOP2 in the simulations.

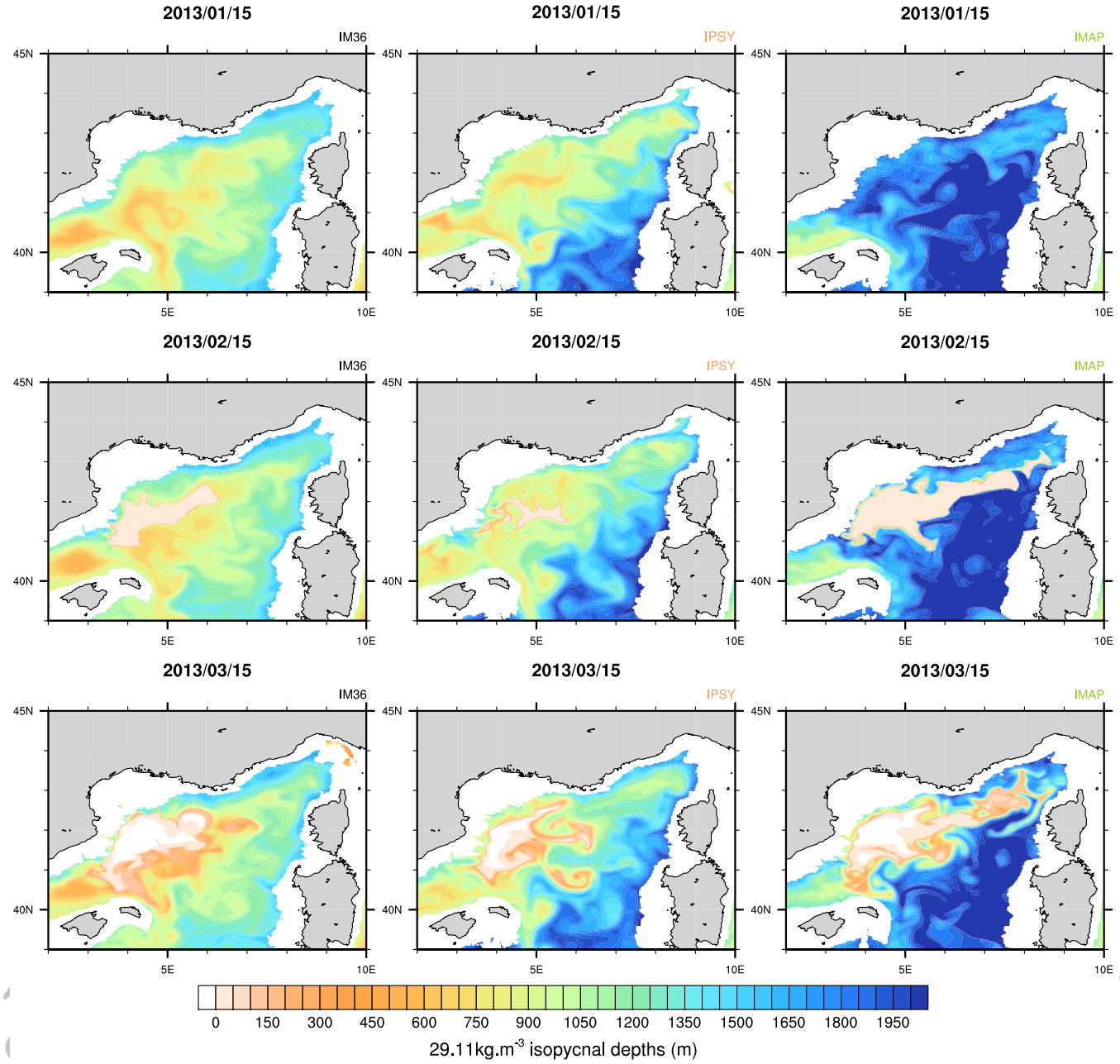

Figure 10. 29.11 kg.m^{-3} isopycnal surface depths (meters) in IM36, IPSY and IMAP for 15 January, 15 February and 15 March 2013.

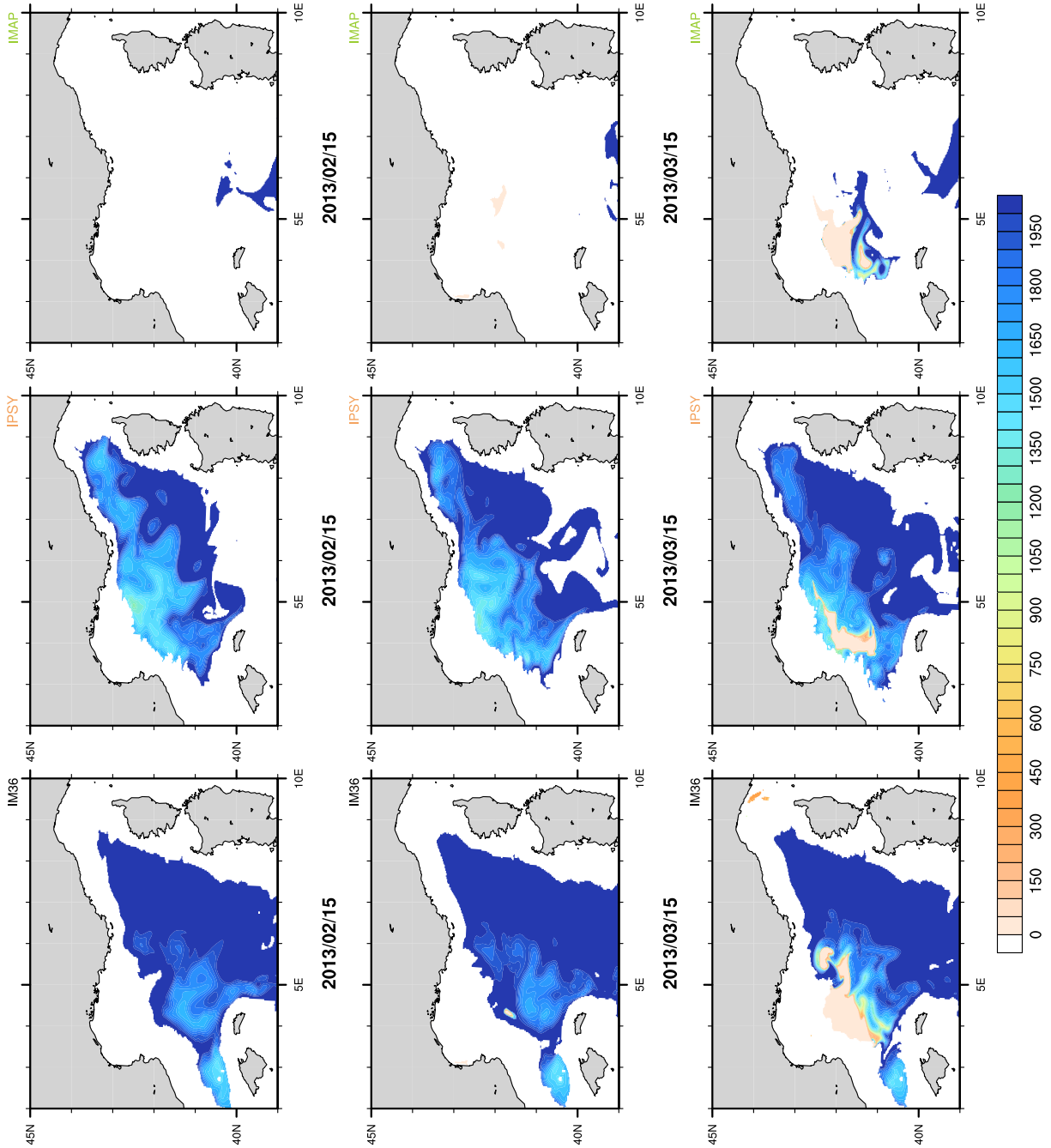

Figure 11. As in Fig. 10 but for the 29.12 $kg.m^{-3}$ isopycnal surfaces.

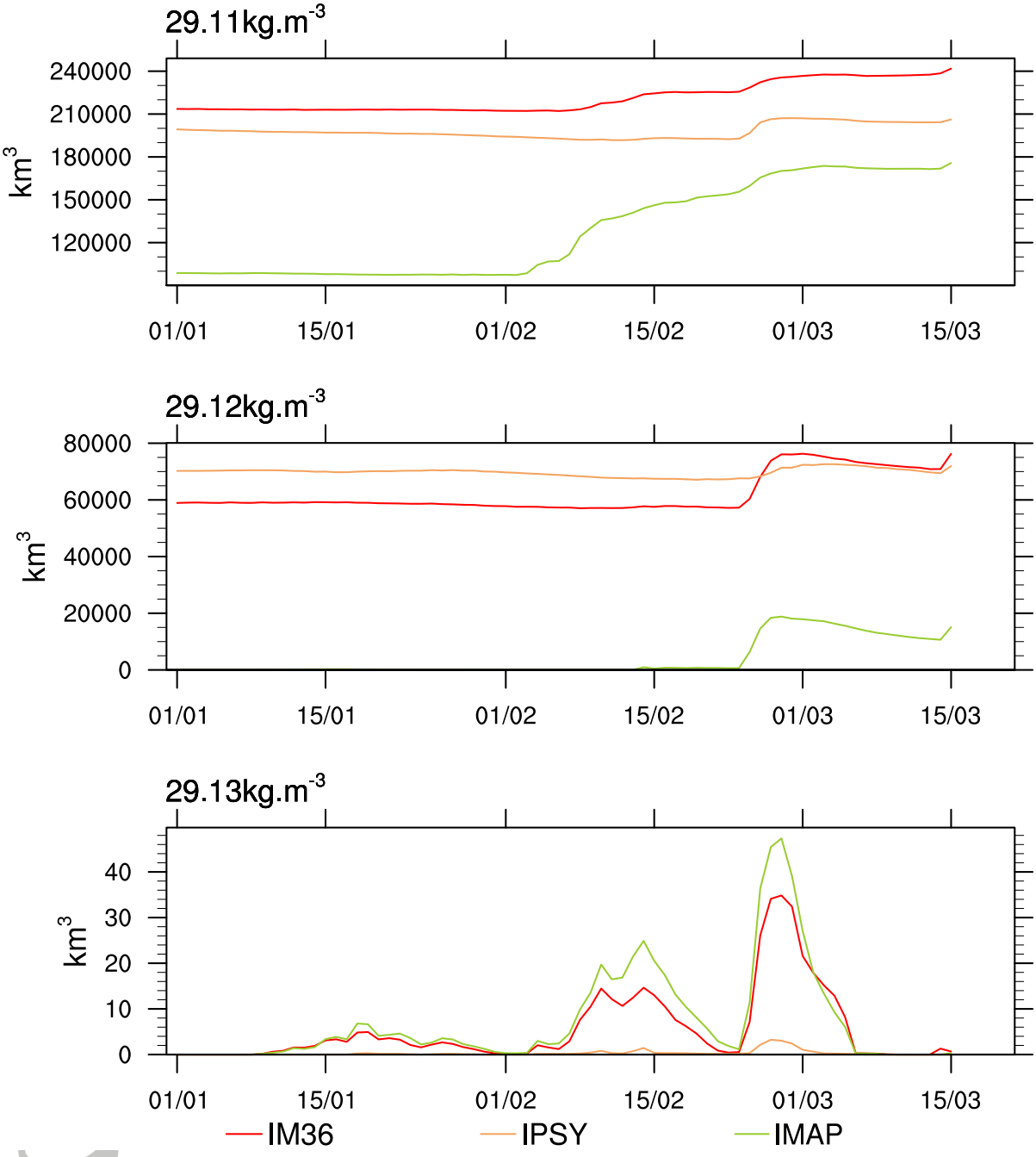

Figure 12. Simulated volumes (km^3) time-series of water denser than 29.11, 29.12 and 29.13 $kg.m^{-3}$ from 1st January to 15 March 2013.

Figure 13. θ/S diagram averaged for SOP2 in the north-western Mediterranean area for the three experiments (top panel) and zoom (dashed rectangle) for the WMDW (bottom panel). The blue rectangle indicates the WMDW (at 1953 m depth) mean characteristics $\pm 2\sigma$ from ARGO float profiles.